

Towards First-principle Characterization of Cosmic-ray Transport Coefficients from Multi-scale Kinetic Simulations

XUE-NING BAI^{1,2}

¹*Institute for Advanced Study, Tsinghua University, Beijing 100084, China*

²*Department of Astronomy, Tsinghua University, Beijing 100084, China*

ABSTRACT

A major uncertainty in understanding the transport and feedback of cosmic-rays (CRs) within and beyond our Galaxy lies in the unknown CR scattering rates, which are primarily determined by wave-particle interaction at microscopic gyro-resonant scales. The source of the waves for the bulk CR population is believed to be self-driven by the CR streaming instability (CRSI), resulting from the streaming of CRs downward a CR pressure gradient. While a balance between driving by the CRSI and wave damping is expected to determine wave amplitudes and hence the CR scattering rates, the problem involves significant scale separation with substantial ambiguities based on quasi-linear theory (QLT). Here we propose a novel “streaming box” framework to study the CRSI with an imposed CR pressure gradient, enabling first-principle measurement of the CR scattering rates as a function of environmental parameters. By employing the magnetohydrodynamic-particle-in-cell (MHD-PIC) method with ion-neutral damping, we conduct a series of simulations with different resolutions and CR pressure gradients and precisely measure the resulting CR scattering rates in steady state. The measured rates show scalings consistent with QLT, but with a normalization smaller by a factor of several than typical estimates based on single-fluid treatment of CRs. A momentum-by-momentum treatment provides better estimates when integrated over momentum, but is also subject substantial deviations especially at small momentum. Our framework thus opens up the path towards providing comprehensive subgrid physics for macroscopic studies of CR transport and feedback in broad astrophysical contexts.

Keywords: Plasma astrophysics (1261) — Alfvén waves (23) — Magnetohydrodynamics (1964) — Cosmic rays(329)

1. INTRODUCTION

Cosmic-rays (CRs) are (trans-)relativistic charged particles traveling through space. They are generated in energetic astrophysical sources, especially shocks from supernova remnants via diffusive shock acceleration (Bell 1978; Blandford & Ostriker 1978; Drury 1983, e.g.). Being energetic particles, CRs naturally tend to escape from acceleration sites. Individual CR particles travel along while gyrating around magnetic field lines, and in the meantime are scattered by waves and turbulence. The intensity of the waves and/or level of turbulence determine how efficiently CRs propagate through the background medium, a process known as CR transport. In the Galaxy, the bulk CR energy density is domi-

nated by protons with \sim GeV energies that are primarily generated from the Galactic disk. They are transported outward, and eventually escape from the Galaxy over a few million years (Ginzburg & Syrovatskii 1964; Strong et al. 2007). Balancing CR production with escape (and to a lesser extent, energy losses), the typical CR energy density found in the interstellar medium (ISM) is of the order $\sim 1 \text{ eV cm}^{-3}$, corresponding to a number density of $n_{\text{CR}} \sim 10^{-9} \text{ cm}^{-3}$ (Grenier et al. 2015).

In the interstellar medium (ISM), CRs are not simply test particles that respond passively to background waves and turbulence. Rather, they are dynamically important with energy density comparable to or exceeding that of other components of the ISM such as thermal gas and magnetic field. As such, the backreaction from the CRs to their host galaxy leads to a number of significant physical consequences, known as CR feedback (see e.g. the reviews of Ferrière 2001; Zweibel 2017; Naab &

Ostriker 2017). The coupling between CRs and background thermal gas is mediated by magnetic fields. Besides pressure support, wave-particle interaction allows CRs to exchange momentum and energy with the waves, and hence the background gas itself, leading to heating and momentum deposition in the ISM, potentially driving galactic winds (e.g., Ipavich 1975; Breitschwerdt et al. 1991; Zirakashvili et al. 1996; Everett et al. 2008; Mao & Ostriker 2018; Hopkins et al. 2021a; Quataert et al. 2022; Huang & Davis 2022).

The most complex but fascinating fact about CR transport and feedback is that the waves that are crucially responsible are considered to be self-generated due to the CR streaming instability (CRSI; [Kulsrud & Pearce 1969](#); [Skilling 1971](#); [Wentzel 1974](#))¹: when the bulk CRs drift (a.k.a. streaming) relative to background gas at a speed v_D that is faster than the Alfvén speed v_A , Alfvén waves become unstable, and grow at the cost of the free energy from CR streaming. The underlying physical mechanism of this so-called CR self-confinement involves the gyro-resonance: particles exchange energy and momentum only to Alfvén waves whose wavelengths are resonant with its gyro-orbit. The growth rate of the CRSI is of the order $\Omega_c(v_D - v_A)(n_{\text{CR}}/n_0)$, where Ω_c is the cyclotron frequency, and n_{CR} , n_0 are number densities of the CRs and background ion plasma. Usually, CR streaming is naturally fed by the CR sources as CRs escape down a CR pressure gradient. The Alfvén waves generated by the CRSI will scatter the CRs, and are expected to isotropize the CR distribution in the wave frame, thus reducing the drift/streaming speed v_D towards v_A .

Accompanying wave growth by the CRSI is wave damping. The damping mechanisms vary with environment, and can be due to ion-neutral collisions ([Kulsrud & Pearce 1969](#); [Soler et al. 2016](#)), non-linear Landau damping ([Lee & Völk 1973](#)), linear Landau damping ([Foote & Kulsrud 1979](#); [Wiener et al. 2018](#)), background turbulence ([Farmer & Goldreich 2004](#); [Lazarian 2016](#)), and (potentially) the role of charged interstellar dust ([Squire et al. 2021](#)). Strong damping can reduce wave amplitudes, making them insufficient to isotropize the CRs. Under quasi-linear theory (QLT), it is often considered that the waves will grow to an extent that partially reduces the effective CR streaming speed so that wave growth balances wave damping in a (quasi-) steady

state ([Kulsrud & Cesarsky 1971](#); [Skilling 1971](#); [Wiener et al. 2013](#)).

CR feedback is often studied at macroscopic level via CR (magneto-)hydrodynamics. The equations are obtained by taking moments at the Fokker-Planck equation for CR transport ([Skilling 1971, 1975](#); [Schlickeiser 2002](#)) and integrating over the CR momentum (grey approximation). The equations are expressed for total CR energy ([McKenzie & Voelk 1982](#); [Guo & Oh 2008](#); [Pfrommer et al. 2017](#)), and more recently also for total CR energy flux ([Jiang & Oh 2018](#); [Thomas & Pfrommer 2019](#); [Chan et al. 2019](#); [Thomas et al. 2021](#)), together with the interaction source terms between gas and the CRs due to CR scattering by the waves. CR scattering is modeled with a prescribed transport coefficient (scattering rate or diffusion coefficient), either isotropic ([Uhlig et al. 2012](#); [Booth et al. 2013](#); [Salem & Bryan 2014](#); [Simpson et al. 2016](#); [Wiener et al. 2017](#)) or field aligned ([Hanasz et al. 2013](#); [Girichidis et al. 2016](#); [Pakmor et al. 2016](#); [Ruszkowski et al. 2017](#)), and is usually treated as a constant that is independent of the physical conditions in the system. Moreover, CRs are often considered as streaming down the CR pressure gradient at a certain streaming speed that is artificially prescribed (e.g., [Ruszkowski et al. 2017](#); [Wiener et al. 2017](#)). As a result, there are substantial degrees of freedom in setting the diffusion coefficients and streaming speeds, which can lead to dramatically different outcomes and hence substantial uncertainties (e.g. [Hopkins et al. 2021b](#)).

Most uncertainties in these macroscopic studies should be resolved at the microscopic level. We note that CRs with a given momentum can interact with waves over a wide range of wavelengths depending on their pitch angle. The interaction of a CR population (with an energy distribution) with waves thus involves complex convolution of wave-particle interactions. The conventional treatment with QLT has to make strong simplifying assumptions in deriving the scattering coefficients, leaving major uncertainties. A kinetic approach is essential to capture the complex interplay between CR particles and waves, determine the full wave spectrum, and hence the CR transport coefficients.

Recently, we carried out the first numerical study of the CRSI, with parameters compatible with those typical in the ISM ([Bai et al. 2019](#)) (hereafter [BOPS19](#)). Keys to this work include the use of magnetohydrodynamic-particle-in-cell (MHD-PIC) method ([Bai et al. 2015](#)), which substantially alleviates the issue of scale separation encountered in conventional PIC methods (see [Holcomb & Spitkovsky 2019](#)), and the implementation of the δf weighting scheme, which dramatically reduces particle noise. We further incorpo-

¹ This is the case for the bulk CR population, whereas scattering of more energetic CRs (above a few hundred GeV, [Blasi et al. 2012](#); [Aloisio et al. 2015](#)) are likely dominated by extrinsic turbulence in the ISM (e.g., [Jokipii 1966](#); [Schlickeiser & Miller 1998](#); [Yan & Lazarian 2002](#)).

rated ion-neutral damping in our follow up work (Plotnikov et al. 2021). With a homogeneous and periodic simulation box, we accurately verified the linear growth rate over a wide range of wavelengths, and precisely tracked the quasi-linear evolution of the particles over a wide range of momenta. We also found that the main obstacle for isotropizing the CRs lies in the crossing of 90° pitch angle where certain nonlinearity must be involved to reflect particles.

We note that realistically, a steady, saturated state of the CRSI is achieved by balancing the driving force of a CR pressure gradient with wave damping. While the periodic setup is useful for verifying the basic physics of the CRSI, such a steady state can never be established: the system saturates as the free-energy from CR streaming is exhausted (i.e., CRs are isotropized in the wave frame).

In this paper, we aim to achieve such a steady state to enable first-principle measurement of CR transport coefficients. For this purpose, we have designed a novel simulation framework which we term as “streaming box” that imposes a fixed CR pressure gradient that constantly drives the growth of the CRSI. It demands simultaneously resolving the gyro-resonant scale while accommodating multiple CR mean free paths, making it is truly multi-scale in nature. As a first study, this paper provides the basic framework, as well as initial results by considering ion-neutral damping. We anticipate this framework to open up the window for more systematic future investigations that would eventually provide a comprehensive subgrid model of microscopic CR transport coefficients as a function of local (but macroscopic) environmental parameters. Such a subgrid model, when fed to CR (magneto-)hydrodynamics, is highly desirable for understanding CR transport and feedback on macroscopic scales over a wide range of astrophysical systems.

This paper is organized as follows. We start by describing the basic streaming box framework and simulation setup in Section 2. A theoretical framework based on QLT is presented in Section 3 to help interpret simulation results. In Section 4, we show simulation results mainly from our fiducial runs. This is followed by a survey of results on CR scattering rates from all simulations in Section 5. Our results are further discussed in Section 6, connecting to CR (magneto-)hydrodynamics. We conclude in Section 7. Additional numerical aspects of our simulations are described in the Appendices.

2. SIMULATION SETUP WITH STREAMING BOX

In this section, we describe a novel simulation framework that we term “streaming box”, which has unique advantages for simulating the CRSI towards saturation

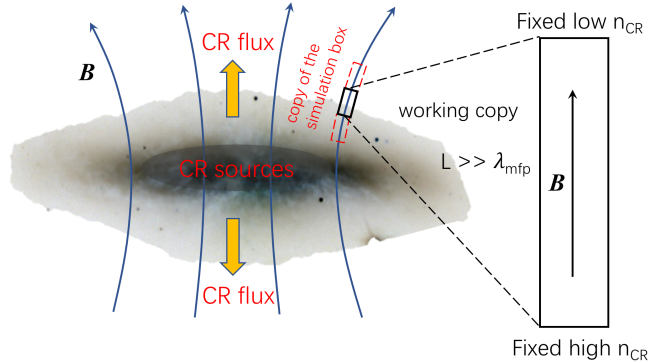


Figure 1. Schematic illustration of the streaming box framework. It can be considered as a local patch embedded in a global setting where CRs escape from the source downward the CR pressure gradient along magnetic fields on macroscopic scales, e.g., in a star-forming galaxy. The box employs periodic boundary conditions for the background gas, while maintaining the global CR pressure gradient by imposing fixed but different CR number densities at the two boundaries. This creates and drives CR streaming through the box, triggering the CRSI to achieve steady state by balancing wave growth and damping. In the meantime, the box size should be sufficiently long to accommodate multiple CR mean free paths at saturated wave amplitudes. See Section 2 for details.

that enables measuring CR scattering rates. Detailed implementation will be given in Appendix A.

2.1. General description of the streaming box framework

The streaming box is a Cartesian simulation box which can be considered as a local patch in a global system where the CRs stream downward a CR pressure gradient (see Figure 1). The box is aligned with the CR pressure gradient and, in this work, we further assume the CR pressure gradient is aligned with the background magnetic field (this can be relaxed when considering multi-dimensional problems). We refer to this direction as the \hat{x} axis, with box size being L_x .

From a macroscopic perspective, the box size L_x should be sufficiently small so that the fractional variation in CR pressure across the box is small, and the background gas properties and magnetic fields can be regarded as approximately uniform.² In other words, $L_x \ll L_{\text{macro}}$, where L_{macro} is some macroscopic scale where CR or background gas properties vary significantly. From microscopic perspective, on the other hand, the box must be long enough to well accommo-

² Arguably, the gradient in background gas density may exceed the background CR pressure gradient. However, it is the CR gradient that plays a driving role that must be kept.

date the CR mean free path, or $L_x \gg \lambda_{\text{mfp}}$, which is essential for CRs to be sufficiently scattered to exhibit fluid-like behavior.

Given $L_x \ll L_{\text{macro}}$, the initial state of the background gas is set to be uniform, employing periodic boundary conditions. For CRs, a pressure gradient is enforced by injecting CR particles from the two box boundaries but at different rates, and is practically achieved by fixing CR number densities at the boundaries (detailed implementation is described in Appendix A.1). In other words, the box is essentially connected to neighboring “boxes” that share similar conditions and maintain similar CR pressure gradient, as depicted in Figure 1. We denote the CR number densities at the higher and lower sides to be $n_{\text{CR}}^{\text{hi}}$ and $n_{\text{CR}}^{\text{lo}}$, respectively, and further define

$$n_{\text{CR}}^{\text{ctr}} = (n_{\text{CR}}^{\text{hi}} + n_{\text{CR}}^{\text{lo}})/2, \quad \Delta n_{\text{CR}} = n_{\text{CR}}^{\text{hi}} - n_{\text{CR}}^{\text{lo}}, \quad (1)$$

as the mean CR number density and density variation in the box. As a local approach, we demand $\Delta n_{\text{CR}} \ll n_{\text{CR}}^{\text{ctr}}$. To facilitate discussion, let our coordinate be chosen such that the left/right boundaries are at $x = 0$ and $x = L_x$, respectively, with high CR pressure on the left ($x = 0$) side. Therefore, we anticipate a steady state CR number density profile $n_{\text{CR},0}(x)$ to be

$$n_{\text{CR},0}(x) = n_{\text{CR}}^{\text{hi}} - (x/L_x)\Delta n_{\text{CR}}. \quad (2)$$

A more subtle requirement is that $\Delta n_{\text{CR}}/n_{\text{CR}}^0 \gg v_A/c$. This is because to trigger the CRSI in the simulation box, there must be some initial anisotropy that exceeds $\sim v_A/c$. The upper limit of anisotropy that can be achieved in the box is the free-streaming limit, which would yield an effective streaming speed on the order of $(\Delta n_{\text{CR}}/n_{\text{CR}}^0)c$ (for relativistic CRs). Therefore, we must allow for larger $\Delta n_{\text{CR}}/n_{\text{CR}}^0$ ratio to accommodate sufficient range of CR streaming speeds.

To summarize, the basic requirements in the streaming box setting are that $\lambda_{\text{mfp}} \ll L_x \ll L_{\text{macro}}$, and $v_A/c \ll \Delta n_{\text{CR}}/n_{\text{CR}}^0 \ll 1$. To some extent, it is analogous to the shearing-box framework in the context of accretion disk simulations (Hawley et al. 1995), where the background gradient is ignored to employ periodic-like boundary conditions, while retaining the driving force (i.e., rotation and shear). Compared to the conventional periodic box setup in BOPS19, the streaming box framework is more computationally demanding in requiring $L_x \gg \lambda_{\text{mfp}} \sim (\delta B/B)^{-2}R_g$, where R_g is CR gyroradius, while the periodic box simply requires $L \gg R_g$ (to properly capture quasi-linear diffusion). We note that the resolution requirement in a periodic box is already demanding, especially due to the need to enable reflection across 90° pitch angle (see BOPS19), the streaming

box setup thus mandates accommodating a hierarchy of well separated scales: $\Delta x \ll R_g \ll \lambda_{\text{mfp}} \ll L_x$. Therefore, the simulations are most affordable in 1D, which is our starting point to investigate the rich kinetic physics.

2.2. The MHD-PIC method

Our simulations are conducted using the Athena MHD code (Stone et al. 2008), supplemented with CR particles to become an MHD-PIC code (Bai et al. 2015). It solves MHD equations for background gas, and simultaneously integrates CR particle trajectories in the MHD electromagnetic field, with backreaction on the background gas. In conservative form, the MHD equations read (BOPS19)

$$\frac{\partial \rho}{\partial t} + \nabla \cdot (\rho \mathbf{v}_g) = 0, \quad (3)$$

$$\begin{aligned} \frac{\partial(\rho \mathbf{v}_g)}{\partial t} + \nabla \cdot (\rho \mathbf{v}_g^T \mathbf{v}_g - \mathbf{B}^T \mathbf{B} + P^* \mathbf{l}) \\ = - (q n_{\text{CR}} \mathcal{E} + \mathbf{J}_{\text{CR}} \times \mathbf{B}), \end{aligned} \quad (4)$$

$$\frac{\partial \mathbf{B}}{\partial t} = \nabla \times (\mathbf{v}_g \times \mathbf{B}), \quad (5)$$

where $P^* \equiv P_g + B^2/2$, $\mathcal{E} \equiv -\mathbf{v}_g \times \mathbf{B}$ is the electric field, \mathbf{l} is the identity tensor. In the above, ρ , \mathbf{v}_g , P_g are gas density, velocity, and pressure. Note we have adopted the units where magnetic permeability is unity so that factors of $(4\pi)^{-1/2}$ that would otherwise appear with magnetic fields are eliminated. As an initial study, we adopt an isothermal equation of state $P = \rho c_s^2$, with isothermal sound speed c_s , avoiding additional complications from heating and cooling (see Appendix C for further discussion). We use the Roe Riemann solver (Roe 1981) and third-order reconstruction in characteristic variables.

For CR particles, let m and q be particle mass and charge. Given particle j , let its velocity and momentum be \mathbf{V}_j and \mathbf{p}_j . For notational convenience, we omit mass in the definition of particle momentum, so that they are related by $\mathbf{p}_j = \gamma_j \mathbf{V}_j$, with Lorentz factor

$$\gamma(p_j) = \frac{\sqrt{\mathbb{C}^2 + p_j^2}}{\mathbb{C}} = \frac{\mathbb{C}}{\sqrt{\mathbb{C}^2 - V_j^2}}, \quad (6)$$

where \mathbb{C} is the (numerical) speed of light for CR particles (valid as long as $\mathbb{C} \gg v_A$ and c_s)³, and particle energy

³ While one can rescale the MHD-PIC equations to conform to the reduce-speed-of-light approximation (Ji & Hopkins 2021), we emphasize that the present formulation is fully valid as long as it ensures sufficient scale separation, and we will see that the dimensionless scattering coefficients are independent of \mathbb{C} .

is $E(p) \equiv \gamma(p)\mathbb{C}^2$. The particle equation of motion is given by

$$\frac{d\mathbf{p}_j}{dt} = \left(\frac{q}{m}\right) \left(\boldsymbol{\varepsilon} + \mathbf{V}_j \times \mathbf{B}\right), \quad (7)$$

and is solved by the standard Boris integrator (Boris 1970), together with a standard triangular-shaped cloud (TSC) scheme (Birdsall & Langdon 2005) for interpolation. We note that in all occasions, q and m can be combined to a single factor (q/m) characterizing the charge-to-mass ratio (Bai et al. 2015, BOPS19). In particular, the CR (non-relativistic) cyclotron frequency is given by $\Omega_c = (q/m)B$.

Backreaction from CRs on the gas is reflected in Equation (4) through the Lorentz force experienced from the CR population. Defining $f(t, \mathbf{x}, \mathbf{p})$ as the CR momentum distribution function (DF), the CR number density n_{CR} and current density \mathbf{J}_{CR} are given by $n_{\text{CR}}(t, \mathbf{x}) = \int f(t, \mathbf{x}, \mathbf{p}) d^3\mathbf{p}$ and $\mathbf{J}_{\text{CR}}(t, \mathbf{x}) = q \int \mathbf{v} f(t, \mathbf{x}, \mathbf{p}) d^3\mathbf{p}$. Assuming background gas has the same composition as CR particles, the magnitude of CR feedback is determined by the normalization of the DF, characterized by n_{CR}/n_i , where $n_i = \rho/m$ is the number density of the background gas.

2.3. Simulation setup

Our streaming box simulations follows a 1D setup along the \hat{x} direction, with uniform background gas density $\rho_0 = 1$, background magnetic field $\mathbf{B}_0 = B_0\hat{x} = 1$. This gives a background Alfvén speed $v_A = B_0/\sqrt{\rho_0} = 1$. We carry our simulations in the frame of forward propagating Alfvén waves, and hence the background gas velocity is set to $\mathbf{v}_{g0} = -v_A\hat{x}$ (see Appendix A.3 for a discussion on the choice of simulation frames). We choose the isothermal sound speed to be $c_s = 1$, so that ion thermal pressure and magnetic pressures are about in equipartition. On top of the background, we initialize a spectrum of Alfvén waves as seed perturbations, with $I(k)$ being the wave intensity at wave number k , normalized by

$$E_{\text{wave}} \equiv \int I(k) dk = \frac{1}{2} \frac{\langle \rho \delta v^2 + \delta B^2 \rangle}{\rho_0 v_{A0}^2} \approx \frac{\delta B^2}{B_0^2}, \quad (8)$$

where angle bracket represents spatial average, and E_{wave} denotes dimensionless wave energy density. We initialize the simulations with four Alfvén wave modes (left/right handed with forward/backward propagation) over all wavelengths that can fit into the simulation box, whose wave intensities are fixed at $kI(k) = 10^{-6}$ for all modes with random phases. Details of wave decomposition are described in Appendix A of BOPS19.

For CR particles, we set their charge-to-mass ratio $q/m = 1$ so that their cyclotron frequency $\Omega_c = qB_0/m = 1$. This choice determines the length unit in the simulations to be $d_i = v_A/\Omega_c = 1$, which we note corresponds to the ion inertial length c/ω_{pi} for the background plasma.⁴ Our MHD-PIC framework is generally applicable on scales greater than d_i . We choose the numerical speed of light to be $\mathbb{C} = 300v_A = 300$, the same as in BOPS19 to achieve sufficient scale separation ($\mathbb{C} \gg v_A$).

We take the mean/central background CR DF $f_0^{\text{ctr}}(p)$ to be a κ distribution, given by

$$f_0^{\text{ctr}}(p) = \frac{n_{\text{CR}}^{\text{ctr}}}{(\pi\kappa p_0^2)^{3/2}} \frac{\Gamma(\kappa + 1)}{\Gamma(\kappa - \frac{1}{2})} \left[1 + \frac{1}{\kappa} \left(\frac{p}{p_0}\right)^2\right]^{-(\kappa+1)}, \quad (9)$$

and in our streaming box setting, the full distribution function has a spatial dependence, given by

$$f_0(x, p) = \frac{n_{\text{CR},0}(x)}{n_{\text{CR}}^{\text{ctr}}} f_0^{\text{ctr}}(p). \quad (10)$$

This DF is mainly characterized by p_0 and κ . It approaches a constant at $p \ll p_0$ and approaches a power-law distribution $f \propto p^{-2(\kappa+1)}$ at $p \gg p_0$. Just as in BOPS19, we choose $\kappa = 1.25$, corresponding to $f_0^{\text{ctr}}(p) \propto p^{-4.5}$ at large p , and set $p_0 = \mathbb{C} = 300$, so that the DF peaks at trans-relativistic CR energies. The resonant wavelength for the bulk CR population is then $\lambda_0 = 2\pi p_0/\Omega_c = 1.885 \times 10^3 d_i$, achieving good scale separation from d_i . In our simulations, we use the δf method which dramatically reduces noise and improves the accuracy, as implemented in BOPS19 for a homogeneous background $f_0(p)$. We discuss in Appendix A.2 about its generalization to the streaming box framework with the background DF inhomogeneous.

To inject CRs following the DF (9), (10), similar to BOPS19, we divide the momentum space into 16 bins from $0.01p_0$ to $100p_0$, with four bins per dex. An equal number (N_p) of CR particles per cell per bin are injected which guarantees a sufficient number of particles in each bin. Within each bin in each cell, particles are sampled according to $f_0(x, p)$ in that momentum range (given by (9) and (10)). By default, we set $N_{\text{ppc}} = 96$ particles per cell (or $N_{\text{ppcb}} = 6$ particles per cell per bin) for a particle DF at the center of the box f_0^{ctr} , and adjust the number of particles per cell based on the cumulative CR column

⁴ This correspondence assumes the CRs and background plasmas share the same composition. Note that we use d_i as our length units mainly for convenience, which is more familiar to the plasma physics community, while we emphasize that our simulations do not capture the kinetic physics of the background plasmas.

density from one of the boundaries to accommodate a CR number density gradient. CR injection at the two boundaries is described in Appendix A.1.

Among several wave damping mechanisms (mentioned in Section 1), we consider ion-neutral damping that dominates in weakly ionized gas as a first study. In this case, the background gas that we simulate represents the ion-fluid. The neutral fluid is considered to be inactive, staying at constant background velocity \mathbf{v}_{g0} (same as the initial ion velocity). We have studied the CRSI with ion-neutral damping in a periodic box in Plotnikov et al. (2021). The damping term is implemented by operator-splitting as

$$\frac{\partial \mathbf{v}_g}{\partial t} = -\nu_{\text{in}}(\mathbf{v}_g - \mathbf{v}_{g0}), \quad (11)$$

where the ions collide with neutrals at frequency $\nu_{\text{in}} = n_n \langle \sigma v \rangle [m_n / (m_n + m_i)]$, here taken to be constant, which drives the ion velocity towards \mathbf{v}_{g0} . In the above, n_n is the number density of the neutrals, and m_i, m_n are the mass of individual ions and neutrals, and $\langle \sigma v \rangle$ is the rate of momentum transfer. This formulation is valid in the high-frequency regime where $\omega = kv_A \gg \nu_{\text{in}}$, generally applicable in the ISM.

2.4. Main parameters and list of runs

Unless otherwise noted, we also fix most of the main control parameters to our simulations to be

- CR number density ratio $n_{\text{CR}}^{\text{ctr}}/n_i = 10^{-4}$.
- CR variation $\Delta n_{\text{CR}}/n_{\text{CR}}^{\text{ctr}} = 0.4$.
- Simulation box size $L_x = 10^7 d_i$.
- Ion-neutral damping rate $\nu_{\text{in}} = 10^{-4} \Omega_c$.

Our choice of box size corresponds to $L_x \sim 5300 \lambda_{\text{res}}$, and hence we can accommodate particles with mean free path up to $\lambda_{\text{mfp}} \sim 10^3 \lambda_{\text{res}}$. This allows us to achieve relatively small wave amplitudes approaching realistic conditions of $\delta B/B_0 \ll 1$. With these, we define the CR scale length

$$L_{\text{CR}} \equiv \frac{n_{\text{CR}}}{\mathbf{b} \cdot \nabla n_{\text{CR}}} \approx \frac{n_{\text{CR}}^{\text{ctr}}}{\Delta n_{\text{CR}}} L_x, \quad (12)$$

which characterizes the spatial gradient of the CR distribution (\mathbf{b} is the unit vector along the magnetic field). Generally, we anticipate $L_{\text{CR}} \approx (n_{\text{CR}}^{\text{ctr}}/\Delta n_{\text{CR}})L_x$, while in practice, as discussed in Appendix A.3 and shown in Section 4.1, the final CR density/pressure gradient will show minor deviations. We thus only conduct measurements around the simulation box center, and report the results based on the locally measured values of L_{CR} there.

The list of all our simulations runs are given in Table 1. By default, we choose the cell size to be $\Delta x = 5d_i$, but also conduct one higher-resolution run with $\Delta x = 2.5d_i$ (run name ‘‘Hires’’) and one lower-resolution run with $\Delta x = 10d_i$ (run name ‘‘Lores’’). This choice corresponds to $\lambda_{\text{res}}/\Delta x \sim 187 - 750$. We will demonstrate that this resolution is sufficient to allow particles to overcome the $\mu = 0$ barrier, and hence we are able to capture the full scattering processes to properly measure the resulting scattering rates. Our simulations are typically run for $1.6 - 2.5 \times 10^5 \Omega_c^{-1}$, which is about 4 – 7 box-crossing time for typical particles, generally sufficient to achieve a steady state.

3. THEORETICAL FRAMEWORK

Before showing simulation results, we lay down a theoretical framework for measuring CR transport coefficients (scattering rates) from our simulations, to be compared with those obtained from QLT.

3.1. Linear instability of waves

Linear growth of CRSI is usually derived in a homogeneous setting with constant CR streaming speed v_D , namely, the CR DF is isotropic in the drift frame. Here, we only summarize the necessary results needed for setting up and analyzing the simulations. For this purpose, we define the wave-frame streaming speed v_s as $v_s = v_D - v_A$. Further details can be found in BOPS19 and Plotnikov et al. (2021). The CRSI drives growth of forward-propagating, both left and right polarized Alfvén waves. They share the same growth rate given by

$$\Gamma_{\text{CR}}(k) \approx \frac{\pi}{4} \frac{n_{\text{CR}}}{n_i} \Omega_c \frac{v_s}{v_A} Q(k), \quad (13)$$

where⁵

$$Q(k) \equiv \int_{p_{\text{res}}}^{\infty} dp \frac{4\pi p^2 f_0(p)}{n_{\text{CR}}} \left(\frac{p_{\text{res}}}{p} \right), \quad (14)$$

and $p_{\text{res}}(k) = \Omega_c/k$ is the minimum CR momentum to resonate with an Alfvén wave with wave number k (at zero pitch angle). Here we use n_{CR} and f_0 to ease our notation, while they should be understood as $n_{\text{CR}}^{\text{ctr}}$ and f_0^{ctr} in our setting. With the κ distribution (9), we have

$$Q(k) = \frac{2}{\kappa^{3/2} \sqrt{\pi}} \frac{\Gamma(\kappa + 1)}{\Gamma(\kappa - \frac{1}{2})} \frac{1}{s(k) [1 + 1/(\kappa s(k)^2)]^\kappa}, \quad (15)$$

where $s(k) \equiv p_0/p_{\text{res}} = kp_0/\Omega_c$. The growth rate peaks at $s = 1$ or $k_0 \equiv \Omega_c/p_0$, namely, at the resonant

⁵ Our definition of $Q(k)$ is a factor $2/\pi$ of $Q_2(k)$ in BOPS19.

Table 1. List of main simulation runs

Run	ν_{in} ($10^{-4}\Omega_c$)	Box size (L_x/d_i)	$\Delta n_{\text{CR}}/n_{\text{CR}}^{\text{ctr}}$	Resolution ($\Delta x/d_i$)	N_{ppc}	Runtime (Ω_c^{-1})	E_{wave} ($\rho_0 v_A^2$)	Δv_g (v_A)	L_{CR} ($10^7 d_i$)	α_{sca}
Fid	1.0	10^7	0.4	5	96	2.0×10^5	2.70×10^{-3}	2.77×10^{-3}	2.39	0.0544
Lores	1.0	10^7	0.4	10	128	2.5×10^5	2.64×10^{-3}	2.71×10^{-3}	2.38	0.0529
Hires	1.0	10^7	0.4	2.5	64	1.6×10^5	2.67×10^{-3}	2.70×10^{-3}	2.40	0.0554
Lograd	1.0	10^7	0.24	5	96	2.5×10^5	1.27×10^{-3}	1.29×10^{-3}	4.92	0.0534
Higrad	1.0	10^7	0.56	5	96	1.8×10^5	3.98×10^{-3}	4.07×10^{-3}	1.63	0.0557
Short	1.0	5×10^6	0.4	5	96	1.8×10^5	5.41×10^{-3}	5.68×10^{-3}	1.21	0.0531
Nu05	0.5	10^7	0.4	5	96	1.8×10^5	5.53×10^{-3}	5.88×10^{-3}	2.31	0.0505

Fixed parameters: $\mathbb{C} = 300v_{A0}$, $p_0 = 300v_{A0}$, $n_{\text{CR}}/n_i = 10^{-4}$. Values in the last four columns correspond to wave intensity, ion-neutral drift velocity, CR scale length and dimensionless CR scattering coefficient, measured at final state of the simulations. Note that the latter two quantities are measured for CRs in the momentum range between $0.1p_0$ and $10p_0$.

wavelength of particles with momentum p_0 , where Q is slightly smaller than order unity (~ 0.36 for $\kappa = 1.25$). Asymptotically, the growth rate scales as $\Gamma(k) \sim k^{2\kappa-1}$ at long-wavelength limit, and as $\Gamma(k) \sim k^{-1}$ at short-wavelength limit (see Figure 3 of BOPS19).

With ion-neutral damping, and focusing on the high-frequency limit ($\omega \gg \nu_{\text{in}}$), the growth rate becomes

$$\Gamma_{\text{tot}}(k) \approx \Gamma_{\text{CR}}(k) - \frac{\nu_{\text{in}}}{2}. \quad (16)$$

Therefore, all waves are simultaneously damped at a constant rate of $\nu_{\text{in}}/2$. No wave growth is expected for $\nu_{\text{in}} > 2\Gamma_{\text{CR}}(k_0)$. Examples can be found in Figure 5 of Plotnikov et al. (2021).

3.2. Fokker-Planck equation in the wave frame

As the CRSI drives wave growth, CRs undergo pitch angle diffusion in the Alfvén wave frame. The DF can be expressed as a function of (p, μ) , where $\mu \equiv \cos \theta$ for pitch angle θ . Because the electric field is zero in the wave frame, results can be analyzed on a momentum-by-momentum basis. Starting from the Fokker-Planck equation (e.g., Jokipii 1966; Kulsrud & Pearce 1969)

$$\frac{\partial f}{\partial t} + \mu V \frac{\partial f}{\partial x} = \frac{\partial}{\partial \mu} \left(D_{\mu\mu} \frac{\partial f}{\partial \mu} \right), \quad (17)$$

where $D_{\mu\mu}$ the pitch angle Fokker-Planck coefficient, given by

$$D_{\mu\mu}(p, \mu) \equiv \left\langle \frac{\Delta \mu^2}{2t} \right\rangle = \frac{1 - \mu^2}{2} \nu_{\mu}(p, \mu), \quad (18)$$

where $\Delta \mu$ denotes $\mu(t_0 + t) - \mu(t_0)$ for individual particles at two different times separated by t , followed by an ensemble average denoted by $\langle \cdot \rangle$, and $\nu_{\mu}(p, \mu)$ is the pitch angle scattering rate.

In QLT, the pitch angle scattering rate is given by

$$\nu_{\mu, \text{QL}}(p, \mu) = \pi \Omega k_{\text{res}} I^{L/R}(k_{\text{res}}), \quad (19)$$

where $k_{\text{res}} \equiv \Omega_c/(p|\mu|)$ is the wave number of the resonant waves. The wave intensity $I(k)$ refers to forward-propagating left/right polarized Alfvén waves, with left modes I^L chosen for $\mu > 0$ and right modes I^R chosen for $\mu < 0$. Also note that $\Omega = \Omega_c/\gamma$ is the gyro-frequency.

A very useful result can be obtained by assuming steady state. Following a more formal derivation in Appendix B, we obtain

$$\nu_{\mu}(p, \mu) \frac{\partial f}{\partial \mu} \approx -V(p) \frac{\partial f}{\partial x}, \quad (20)$$

This relation will allow us to directly measure $\nu_{\mu}(p, \mu)$ at the saturated state of our simulations. By comparing this result with (19), it will allow to further constrain the contributions from non-linear effects.

3.3. Moment equations

By integrating Equation (17) over μ , we obtain

$$\frac{\partial F_0}{\partial t} + V(p) \frac{\partial F_1}{\partial x} = 0, \quad (21)$$

where the zeros and first moments of the DF are

$$F_0(x, p) \equiv \frac{1}{2} \int_{-1}^1 f(x, p, \mu) d\mu, \quad (22)$$

$$F_1(x, p) \equiv \frac{1}{2} \int_{-1}^1 \mu f(x, p, \mu) d\mu.$$

Note F_0 is expected to be close but not necessarily the same as the f_0 part of the δf weighting scheme (due to relaxation near the boundaries), and the first moment F_1 reflects the level of anisotropy in the streaming CRs.

By further multiplying μ to Equation (17) and then integrating over μ , we obtain

$$\frac{\partial F_1}{\partial t} + \frac{V(p)}{3} \frac{\partial F_0}{\partial x} = - \int_{-1}^1 \frac{\partial f}{\partial \mu} \frac{1 - \mu^2}{4} \nu_\mu(p, \mu) d\mu, \quad (23)$$

where we have assumed the second moment satisfies

$$F_2(x, p) \equiv \frac{1}{2} \int_{-1}^1 \mu^2 f(x, p, \mu) d\mu \approx \frac{1}{3} F_0, \quad (24)$$

an assumption that holds when f is close to isotropic, in line with the streaming box setup. Still, this equation is not closed as the right hand side of the equation depends on the details of the DF.

To proceed, the most common approach is to truncate the expansion in $f(x, p, \mu)$ to lowest order, and write

$$f(x, p, \mu) \approx F_0(x, p) + 3\mu F_1(x, p), \quad (25)$$

which is known as the Eddington approximation (e.g. Thomas & Pfrommer 2019), and Equation (23) becomes

$$\begin{aligned} \frac{\partial F_1}{\partial t} + \frac{V(p)}{3} \frac{\partial F_0}{\partial x} &\approx -\nu_{\text{Edd}}(p) F_1, \\ \nu_{\text{Edd}}(p) &\equiv \frac{3}{4} \int_{-1}^1 (1 - \mu^2) \nu_\mu(p, \mu) d\mu. \end{aligned} \quad (26)$$

In QLT, if we assume $\nu_\mu(p, \mu) = \nu_\mu(p, -\mu)$, i.e., left/right handed waves have equal power, and that $I(k) \propto k^{-q}$ over some range of k around k_0 , then for a given p around p_0 , we may write $\nu_\mu(p, \mu) = \nu_0(p) |\mu|/p_0)^{q-1} / \gamma(p)$, where $\nu_0 \equiv \pi \Omega_c k_0 I(k_0)$, and this yields

$$\nu_{\text{Edd}}(p) \approx \frac{3}{q(q+2)} \frac{\nu_0}{\gamma(p)} \left(\frac{p}{p_0} \right)^{q-1}. \quad (27)$$

In reality, the Eddington approximation does not necessarily hold, as we will show from our simulations.

In saturated (steady) state of our simulations, we can measure effective scattering rate $\nu_{\text{sca}}(p)$, and the associated CR mean free path $\lambda_{\text{mfp}}(p)$, as

$$\nu_{\text{sca}}(p) \equiv - \frac{V(p)}{3F_1(p)} \frac{\partial F_0(p)}{\partial x} \Rightarrow \lambda_{\text{mfp}}(p) = \frac{V(p)}{\nu_{\text{sca}}(p)}. \quad (28)$$

By comparing $\nu_{\text{sca}}(p)$ with $\nu_{\text{Edd}}(p)$, we will be able to assess how deviations from the Eddington approximation affect the estimation of scattering rates. The parallel diffusion coefficient $D_x(p)$ is related to $\nu_{\text{sca}}(p)$ by

$$D_x(p) = \frac{1}{3} \lambda_{\text{mfp}}(p) V(p) = \frac{V(p)^2}{3\nu_{\text{sca}}(p)}. \quad (29)$$

Given the one-to-one correspondence with $D_x(p)$, we here primarily use $\nu_{\text{sca}}(p)$ in our discussion.

3.4. CR (magneto-)hydrodynamics in the wave frame

The moment equations above can be equivalently expressed in terms of CR hydrodynamics, given by

$$\frac{\partial \epsilon_{\text{CR}}}{\partial t} + \frac{\partial \mathcal{F}_{\text{CR}}}{\partial x} = 0. \quad (30)$$

$$\begin{aligned} \frac{\partial \mathcal{F}_{\text{CR}}}{\partial t} + \mathbb{C}^2 \frac{\partial P_{\text{CR}}}{\partial x} &\equiv -\nu_{\text{sca}}(p) \mathcal{F}_{\text{CR}} \\ &= -4\pi p^3 v(p) E(p) \int_{-1}^1 \frac{\partial f}{\partial \mu} \frac{1 - \mu^2}{4} \nu(p, \mu) d\mu. \end{aligned} \quad (31)$$

where the CR energy density ϵ_{CR} , CR energy flux \mathcal{F}_{CR} , and CR pressure P_{CR} , are defined as⁶

$$\begin{aligned} \epsilon_{\text{CR}} &= \int d^3 \mathbf{p} E(p) f(x, \mathbf{p}) \equiv \int \epsilon_{\text{CR}}(p) d \ln p, \\ \mathcal{F}_{\text{CR}} &= \int d^3 \mathbf{p} \mu V(p) E(p) f(x, \mathbf{p}) \equiv \int \mathcal{F}_{\text{CR}}(p) d \ln p, \\ P_{\text{CR}} &= \int d^3 \mathbf{p} \mu^2 V(p) p f(x, \mathbf{p}) \equiv \int P_{\text{CR}}(p) d \ln p, \end{aligned} \quad (32)$$

where

$$\begin{aligned} \epsilon_{\text{CR}}(p) &= 4\pi p^3 E(p) F_0(p), \\ \mathcal{F}_{\text{CR}}(p) &= 4\pi p^3 V(p) E(p) F_1(p), \\ P_{\text{CR}}(x, p) &= \frac{4\pi}{3} p^4 V(p) F_0(p) = \frac{1}{3} \frac{V^2}{\mathbb{C}^2} \epsilon_{\text{CR}}(p). \end{aligned} \quad (33)$$

Note that the definition of CR pressure implicitly assumes that CR anisotropy is small ($\mathcal{F}_{\text{CR}} \ll \epsilon_{\text{CR}} \mathbb{C}$, similar to the relation between F_2 and F_0). Below, without loss of clarity, we do not distinguish between momentum-integrated ϵ_{CR} and $\epsilon_{\text{CR}}(p)$, etc.

Under CR hydrodynamics, it allows us to define the momentum-integrated effective scattering rate with a physically-meaningful weighting

$$\nu_{\text{sca}} = \frac{\int \nu_{\text{sca}}(p) \mathcal{F}_{\text{CR}} d \ln p}{\int \mathcal{F}_{\text{CR}} d \ln p} = - \frac{\frac{\partial}{\partial x} \int V(p)^2 \epsilon_{\text{CR}} d \ln p}{3 \int \mathcal{F}_{\text{CR}} d \ln p}. \quad (34)$$

Due to limited dynamical range, our simulations can only provide reliable measurements of $\nu_{\text{sca}}(p)$ over finite range of CR momentum. Therefore, we typically only conduct the p -integral over the range $0.1p_0 \leq p \leq 10p_0$. Since CRs over this range are expected to be more efficiently scattered, it overestimates ν_{sca} by a factor of $\gtrsim 2$, as will be discussed in Section 5.2.

⁶ In CR hydrodynamics, ϵ_{CR} , \mathcal{F}_{CR} are often defined in observer's frame. By noting that $(\epsilon_{\text{CR}}, \mathcal{F}_{\text{CR}})$ is a four-vector, our equations can be easily transformed to different frames.

3.5. Piecing together: theoretical expectations

The saturated state in our streaming box setting is achieved by balancing the rate of wave growth and damping. Such an approach is broadly referred to as being based on QLT in the literature.⁷ In practice, however, there are substantial uncertainties pertaining to the exact approximations made to the derivation, leading to wildly different results. Here we roughly divide the treatments in the literature into two categories, namely, treating the CRs as a single fluid (Section 3.5.1) and treating the CRs momentum by momentum (Section 3.5.2).

The starting point is by defining the effective streaming speed v_s^{eff} , which is needed to estimate wave growth rate. From a fluid point of view, we can associate v_s^{eff} with the energy flux \mathcal{F}_{CR} by

$$\begin{aligned}\mathcal{F}_{\text{CR}}(p) &= v_s^{\text{eff}}(p)[\epsilon_{\text{CR}}(p) + P_{\text{CR}}(p)] , \\ \mathcal{F}_{\text{CR}} &= v_s^{\text{eff}}(\epsilon_{\text{CR}} + P_{\text{CR}}) .\end{aligned}\quad (35)$$

From the definitions (33), the above can be expressed as

$$\begin{aligned}v_s^{\text{eff}}(p) &= V(p) \frac{3\mathbb{C}^2}{3\mathbb{C}^2 + V(p)^2} \frac{F_1(p)}{F_0(p)} , \\ v_s^{\text{eff}} &= \frac{\int V(p)p^2 E(p) F_1(p) dp}{\int p^2 [E(p) + Vp/3] F_0(p) dp} .\end{aligned}\quad (36)$$

We remind the readers that here v_s^{eff} is defined in the wave frame.

We shall see in the discussion below that the CR scattering rate should be normalized by

$$\nu_{\text{norm}} \equiv \left(\frac{\mathbb{C}}{v_A} \right) \left(\frac{\mathbb{C}}{L_{\text{CR}} \nu_{\text{in}}} \right) \left(\frac{n_{\text{CR}}^{\text{ctr}}}{n_i} \right) \Omega_c , \quad (37)$$

which reflects the scaling from QLT. We write

$$\nu_{\text{sca}} = \alpha_{\text{sca}} \nu_{\text{norm}} , \quad \nu_{\text{sca}}(p) = \alpha_{\text{sca}}(p) \nu_{\text{norm}} . \quad (38)$$

Calibrating α_{sca} and $\alpha_{\text{sca}}(p)$ is one major goal of our simulations.

3.5.1. Treating CRs as a single fluid

In this first approach, there is a single streaming speed v_s^{eff} , and transport coefficients are derived by balancing growth and damping at the most unstable wavelength.

⁷ As we only consider ion-neutral damping here, which is a linear damping mechanism, QLT is in fact barely utilized in the derivation, making the derivation less uncertain. When non-linear damping mechanisms, such as non-linear Landau damping is considered, one would have to explicitly account for amplitude-dependent scattering rates based on QLT. This is left for our future work.

From (13), with the most unstable $k_0 = \Omega_c/p_0$, we may approximately express the peak CRSI growth rate as

$$\Gamma_{\text{CR}}^{\text{eff}}(k_0) \approx \frac{\pi}{4} \frac{n_{\text{CR}}}{n_i} \Omega_c \frac{v_s^{\text{eff}}}{v_A} Q(k_0) = 0.28 \frac{n_{\text{CR}}}{n_i} \Omega_c \frac{v_s^{\text{eff}}}{v_A} . \quad (39)$$

Balancing the above with ion-neutral damping rate $\Gamma_{\text{damp}} = \nu_{\text{in}}/2$, we obtain for the effective streaming speed (see also Plotnikov et al. 2021):

$$v_{s,1}^{\text{eff}} \approx \frac{2}{\pi Q(k_0)} \frac{\nu_{\text{in}}}{\Omega_c} \frac{n_i}{n_{\text{CR}}} v_A \approx 1.8 \frac{\nu_{\text{in}}}{\Omega_c} \frac{n_i}{n_{\text{CR}}} v_A . \quad (40)$$

This is a theoretical expectation commonly employed in the literature (e.g., Wiener et al. 2013). In particular, as a linear damping mechanism, this expected streaming speed is independent of the imposed CR gradient (Skilling 1971; Kulsrud & Cesarsky 1971).

Combining Equations (34) and (35), we establish the relation

$$\nu_{\text{sca},1}^{\text{pred}} = \frac{\int V(p)^2 \epsilon_{\text{CR}} d \ln p}{3 v_{s,1}^{\text{eff}} L_{\text{CR}} \int (\epsilon_{\text{CR}} + P_{\text{CR}}) d \ln p} \equiv \alpha_{\text{sca},1}^{\text{pred}} \nu_{\text{norm}} , \quad (41)$$

where the dimensionless prefactor is given by

$$\alpha_{\text{sca},1}^{\text{pred}} = \frac{\pi}{2} Q(k_0) \frac{\int V(p)^2 \epsilon_{\text{CR}} d \ln p}{\int (3\mathbb{C}^2 + V(p)^2) \epsilon_{\text{CR}} d \ln p} , \quad (42)$$

which we find to be 0.124 for our choice of the DF.

3.5.2. Treating CRs momentum by momentum

Alternatively, one can treat CRs momentum-by-momentum, each having their own drift speed $v_s^{\text{eff}}(p)$. To approximate wave growth rate at wave number k , we treat particles with $p \geq p_{\text{res}}(k)$ as sharing the same streaming velocity $v_s^{\text{eff}}(p_{\text{res}})$, and write

$$\Gamma_{\text{CR}}^{\text{pred}}(k) \approx \frac{\pi}{4} \frac{n_{\text{CR}}}{n_i} \Omega_c \frac{v_s^{\text{eff}}(p_{\text{res}})}{v_A} Q(k) , \quad (43)$$

where we use the resonance condition $p_{\text{res}} = \Omega_c/k$, or $k_{\text{res}} = \Omega_c/p$, and the $Q(k)$ factor approximately encapsulates the contribution from all particles to the growth at that wavelength. Such approach has been employed in the recent literature to study the role of self-confinement on CR transport (Amato & Blasi 2018; Evoli et al. 2018), but we note that except for Armillotta et al. (2021) who adopted almost identical formulation, our formula is more accurate than those commonly employed⁸.

⁸ Our formula is largely identical to those adopted in the literature except for the $Q(k)$ factor defined in (14), as opposed to the commonly-used $n_{\text{CR}}(p > p_{\text{res}})/n_{\text{CR}}$, or $4\pi p^3 f(p)/n_{\text{CR}}$.

Balancing (43) with damping rate $\Gamma_{\text{damp}} = \nu_{\text{in}}/2$, we obtain the predicted streaming speed as

$$v_{s,2}^{\text{eff}}(p) = \frac{2}{\pi} \frac{\nu_{\text{in}}}{\Omega_c} \frac{n_i}{n_{\text{CR}}} Q(k_{\text{res}})^{-1} v_A. \quad (44)$$

With Equation (31), taking $\partial/\partial t = 0$ for steady state, and expecting $\partial/\partial x \approx -L_{\text{CR}}^{-1}$, we find

$$v_s^{\text{eff}}(p) \approx \frac{V(p)^2}{3\nu_{\text{sca}}(p)} \frac{1}{L_{\text{CR}}} \frac{\epsilon_{\text{CR}}(p)}{\epsilon_{\text{CR}}(p) + P_{\text{CR}}(p)} \quad (45)$$

for individual CR momentum. Equating the above two expressions, we find the predicted scattering rate

$$\nu_{\text{sca},2}^{\text{pred}}(p) = \frac{\pi}{2} Q(k_{\text{res}}) \frac{V(p)^2}{3\mathbb{C}^2 + V(p)^2} \nu_{\text{norm}} \equiv \alpha_{\text{sca},2}^{\text{pred}}(p) \nu_{\text{norm}}. \quad (46)$$

Note the close similarity of $\alpha_{\text{sca},2}^{\text{pred}}(p)$ with (41) and (42) since they are derived based on the same principles.

Note that it is largely identical to Equation (17) of Armillotta et al. (2021) except that they took the last factor to be $3/4$ assuming $V(p) = \mathbb{C}$. Here, we assume L_{CR} for particles of all energies are the same, set by $n_{\text{CR}}^{\text{ctr}}/\Delta n_{\text{CR}} L$ in our case. Given the scalings in our adopted κ -distribution, we have $v_{s,2}^{\text{eff}}(p) \propto p^{-1}$, $\nu_{\text{sca},2}^{\text{pred}}(p) \sim p^3$ at $p \ll p_0$ and $v_{s,2}^{\text{eff}}(p) \propto p^{2\kappa-1}$, $\nu_{\text{sca},2}^{\text{pred}}(p) \sim p^{1-2\kappa}$ at $p \gg p_0$. Note that with this estimate, $v_{s,2}^{\text{eff}}(p)$ diverges at both large and small p .

Integrating the above over momentum, we obtain

$$\nu_{\text{sca},2}^{\text{pred}} \approx \frac{1}{3L_{\text{CR}}} \frac{\int V(p)^2 \epsilon_{\text{CR}}(p) d \ln p}{\int [\epsilon_{\text{CR}}(p) + P_{\text{CR}}(p)] v_{s,2}^{\text{eff}}(p) d \ln p}, \quad (47)$$

which then yields a relation similar to Equation (41). However, the resulting prefactor $\alpha_{\text{sca},2}^{\text{pred}}$ does not converge with the upper momentum bound of the integral, as the denominator scales as $\int p d \ln p$ which quickly diverges (the results are extremely insensitive to the lower-bound of the integral). In reality, this issue can be resolved as scattering by external turbulence will take over beyond some momentum, which can be treated as an effective truncation at some p_{max} . We obtain $\alpha_{\text{sca},2}^{\text{pred}} = 0.046$ for $p_{\text{max}} = 10p_0$, and $\alpha_{\text{sca},2}^{\text{pred}} = 0.0064$ for $p_{\text{max}} = 100p_0$. In either case, the value of $\alpha_{\text{sca},2}^{\text{pred}}$ is much smaller than our previous single-fluid estimate, again reflecting dramatic uncertainties.

4. SIMULATION RESULTS: FIDUCIAL RUN

In this section, we focus on our fiducial run and discuss in detail the physics of the CRSI driven by an imposed background CR gradient.

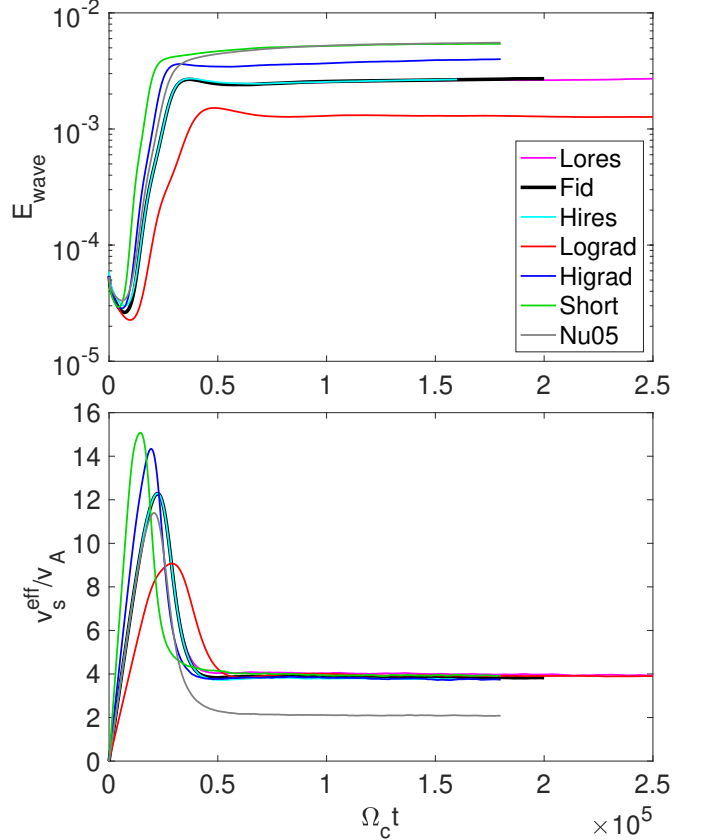


Figure 2. Time evolution of the wave energy density (top) and effective streaming speed (bottom) from all our simulations. In the bottom panel, we show v_s^{eff} defined by Equation (35), averaged over momentum $0.1p_0 < p < 10p_0$.

4.1. Overall evolution

In Figure 2, we show the time evolution of wave energy density and the effective CR streaming speed v_s^{eff} (measured in the simulation frame from (35), i.e., the wave frame) for all simulation runs. Here, the dimensionless wave energy density is defined as $E_{\text{wave}} = (\rho v_{\perp}^2 + B_{\perp}^2)/(2\rho v_A^2)$, and we focus on the the fiducial run in this section (black line). In the meantime, we show in Figure 3 snapshots of the distribution function measured at the central region of the simulation box in the wave frame. It is shown in the form of $\delta f/f_0$ as a function of (p, μ) , where grey indicates isotropy.

Initially, wave energy decreases because of wave damping. Particles are initially isotropic in the wave frame with $v_s^{\text{eff}} = 0$. The background pressure gradient leads to rapid development of CR streaming, with v_s^{eff} increasing linearly in time. This is better viewed from the first panel of Figure 3, showing an excess of particles with $\mu > 0$ and deficit of particles with $\mu < 0$. This triggers the CRSI, and wave energy undergoes exponential growth shortly afterwards.

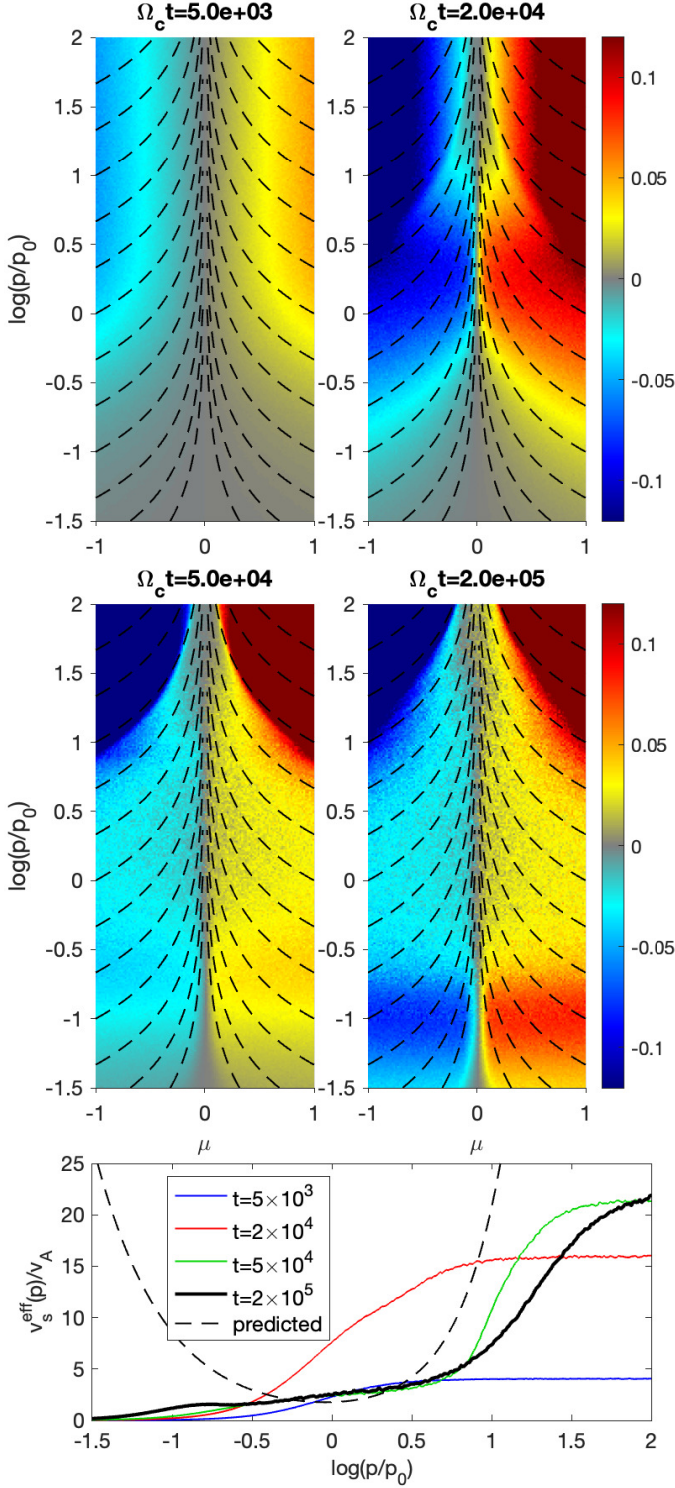


Figure 3. Anisotropy in the CR distribution function, shown as $\delta f(p, \mu)$, at four different simulation snapshots from the fiducial run. The bottom panel shows the effective streaming speed for each particle momentum at these snapshots, over-plotted with the predicted curve given by Equation (44) in dashed line.

As wave amplitude increases, wave-particle interactions scatter the particles and drive the CR population towards isotropy in wave frame. As a result, it slows down and eventually reverses the growth of v_s^{eff} . The overshoot of v_s^{eff} is an inevitable consequence of this initial relaxation process, reaching a maximum value of about $15v_A$. Seen in Figure 3, for particles with momentum around $p = p_0$, level of anisotropy is the highest around time $2 \times 10^4 \Omega_c^{-1}$, and it is substantially reduced by the time of $5 \times 10^4 \Omega_c^{-1}$.

After about $5 \times 10^4 \Omega_c t$, a quasi-stationary state is established, where v_s^{eff} about stays at a constant of $\sim 4v_A$, with wave growth and IN damping balancing each other. The system still evolves afterwards, with wave energy very slowly increasing over time, accompanied by a slow reduction of v_s^{eff} . This is a result of the development of the CRSI towards longer wavelengths, together with the response from more energetic particles that they resonate with. We see from Figure 3 that $\delta f/f_0$ has hardly changed for particles near momentum $p \sim p_0$, but the level of anisotropy is further reduced for particles with $p \sim 10p_0$.

Next, we examine the bulk properties of the CRs and waves in the spatial domain in Figure 4. As discussed in Appendix A.3, there can be some small mismatch at the boundaries, and the CR pressure gradient in the box does not necessarily match what we impose. More quantitatively, the gradient is reflected in the value of L_{CR} from Table 1. For the fiducial run, our imposed gradient would yield $L_{\text{CR}} = 2.5 \times 10^7$, and we see that the actual gradient in the box center is slightly steeper, with deviation less than 10%. Similarly, the spatial distribution of wave energy ($\int I(k) dk = \langle \delta B^2 / B_0^2 \rangle$) is not exactly uniform, where it is about twice in central region than that at the two boundaries. For this reason, all our measurements will be conducted in the central region of the box between the interval $[3 \times 10^6, 7 \times 10^6]$ as marked by vertical dashed lines.

The bottom panel of Figure 4 shows the effective streaming speed calculated from $\mathcal{F}_{\text{CR}} / (\epsilon_{\text{CR}}^{\text{ctr}} + P_{\text{CR}}^{\text{ctr}})$ over the CR population with $0.1p_0 < p < 10p_0$. Note the denominator represents values at domain center (independent of x). The fact that it is flat suggests the system has well arrived at steady state, due to Equation (30).

4.1.1. CR streaming speed

By examining all simulation runs in the bottom panel of Figure 2, we see that except for run Nu05, v_s^{eff} converges to almost the same value at saturated state. This is consistent with the expectation that under linear (ion-neutral) damping, the effective streaming speed should be independent of the imposed CR pressure gradient.

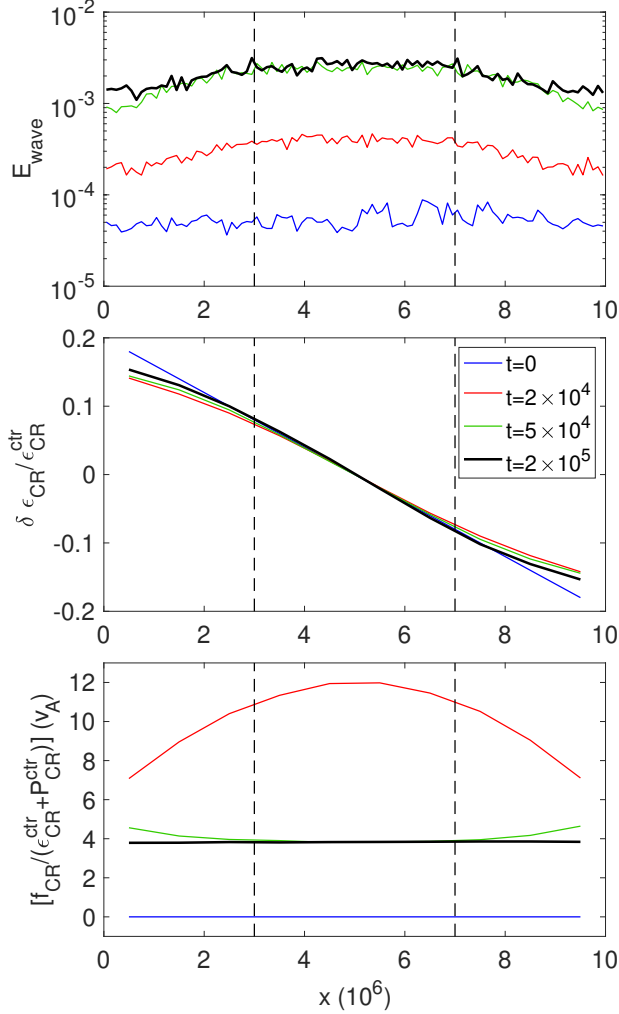


Figure 4. The radial profiles of wave energy density (top), CR energy density (deviation from mean, middle), and the CR streaming speed (bottom) from run Fid. In the middle and bottom panels, only CRs with momentum between $0.1p_0$ and $10p_0$ are counted. Results are shown at four different snapshots indicated in legend.

However, there are substantial mismatches from our theoretical estimates in Section 3.5 in two aspects.

First, the converged value of v_s^{eff} of $\sim 4v_A$ is larger than the expected value of $1.8v_A$ from (40) by a factor of ~ 2 . The higher value of v_s^{eff} indicates that equating *maximum* growth rate with damping rate, does not lead to a balance, but rather, modes at almost all wavelengths will be damped. Therefore, larger v_s^{eff} is needed so that wave amplitudes of a broad range of wavelengths can be maintained. It needs to be a factor of ~ 2 when consider particles in the range of $0.1p_0 < p < 10p_0$, and the difference would be even more if extending to higher-energy particles.

Second, by examining the bottom panel of Figure 3, we see that the predicted momentum-dependent CR streaming speed (44) strongly deviates from our self-consistent measurements: it underestimates v_s^{eff} at p near p_0 , but substantially overestimates v_s^{eff} at smaller and larger p , even excluding regions with $p \lesssim 0.1p_0$ and $p > 10p_0$ not well resolved/accommodated in our simulations. This is likely the consequence of not capturing the complex wave-particle interaction over broad wavelengths and particle momenta.

Finally, we observe that the simulation with ν_{in} reduced by half (run Nu05) leads to a smaller v_s^{eff} smaller than that in other runs also by half, exactly as expected.

4.2. Wave spectrum

The wave pattern and wave energy spectrum from our fiducial run are shown in Figure 5. The waves are decomposed into left/right polarized Alfvén waves following the procedures in BOPS19, and here we have further incorporated the sound waves. At early time of $t = 2 \times 10^4 \Omega_c^{-1}$, the waves grow the fastest at wave number around $k_x = k_0 = \Omega_c/p_0$, corresponding to wavelength $\lambda_0 = 2\pi/k_0$. Both left and right polarized, forward-propagating Alfvén waves are excited at the same rate, as expected.

Around time $t = 5 \times 10^4 \Omega_c^{-1}$, the energy spectrum of the high- k modes (with $k \gtrsim k_0$) are well established in the form of a power-law with $I(k) \propto k^{-1.7}$, mimicking a wave cascade that transfers the energy at $k \sim k_0$ to smaller scales. This process appears strong enough to dominate over the driving from the CRSI itself, and the overall wave energetics is thus determined by this energy transfer and the ion-neutral damping. In Plotnikov et al. (2021), we speculated that it is likely the result of nonlinear steepening of Alfvén waves into rotational discontinuities (Cohen & Kulsrud 1974). Such rotational discontinuities are readily visible in the middle left panel of Figure 5 at multiple locations over a short segment of the simulation box, where one or both of the perpendicular components of the magnetic field can change abruptly, whereas changes in the magnitude of B_{\perp} is much more modest at these locations. We expect it to play a major role helping particles scatter across the 90° pitch angle, as discussed in BOPS19. The high- k end of the spectrum is subject to numerical dissipation, corresponding to the transition to steeper slope at around $k \sim 0.2$, or a wavelength of $\sim \lambda_0/60$ (resolved by $\sim 6 - 7$ cells). We will see that this level of resolution is generally sufficient for convergence for the bulk particle population with $p \gtrsim p_0$.

At later time, lower- k modes gradually catch up, as CRSI modes grow more slowly towards longer wave-

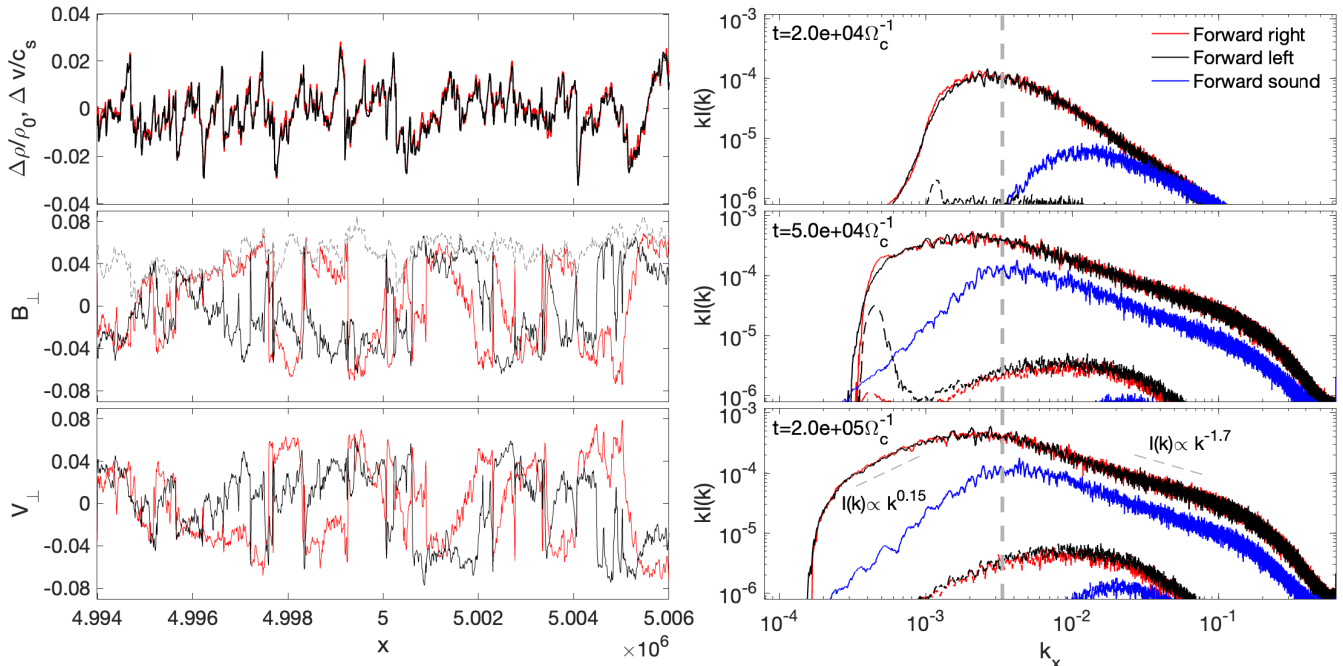


Figure 5. Left: profiles of density (top), longitudinal (top) and perpendicular (bottom) velocity and magnetic field (middle) fluctuations in the very central region of the simulation box, at the end of the fiducial simulation, showing typical wave patterns. Also shown in the middle panel is the magnitude of perpendicular field in grey dashed line. Right: spectrum of the waves, shown as dimensionless wave intensity $kI(k)$ at three different snapshots (from top to bottom). Waves are decomposed into left/right polarized Alfvén waves and sound waves. Forward/backward propagating waves are shown in solid/dashed lines. The vertical dashed line mark the wave number resonating with particles with $p = p_0$ at zero pitch angle.

lengths. Note that by showing the dimensionless $kI(k)$, the lines in the right panels of Figure 5 directly indicate the energetics of individual modes. The spectrum peaks between $k \sim (0.5-1)k_0$, and drops towards longer wavelengths mainly as a result of fewer CRs energetic enough to resonantly interact with these waves. The system develops a different power law with $I(k) \propto k^{0.15}$ over a relatively short range between $k_x \sim 0.1 - 0.5k_0$.

In steady state, the wave spectrum rapidly drops and cuts off at $k \lesssim k_{\min} = 2 \times 10^{-4}$, or $\sim 0.06k_0$. This cutoff is physical due to ion-neutral damping. As a result, there is not much isotropization for particles with $p \gtrsim 10p_0$. To examine this, we may set $v_s^{\text{eff}} \sim 15v_A$ as mean value for particles with $p \gtrsim 10p_0$, as seen from the bottom panel of Figure 3. By requiring $\Gamma_{\text{CR}} > \nu_{\text{in}}/2 = 0.5 \times 10^{-4}$, we find $k \gtrsim 0.06k_0$, which agrees well with the cut-off observed in the wave spectrum.

Interestingly, we also observe the growth of forward-propagating sound waves, initially at high- k and later extending to lower- k covering most of the wavelengths where the CRSI operates. The wave energy spectrum of the sound waves run parallel with the Alfvén waves at high- k while being lower by a factor of ~ 2 , indicative of similar origin (also present though not discussed in our previous studies, in BOPS19, Plotnikov et al.

2021; Bambic et al. 2021). It is also unsurprising, as the CRSI primarily excites linearly-polarized Alfvén waves (left/right modes share similar amplitudes) that lead to variations in perpendicular magnetic pressure. We anticipate that the sound waves have minimum influence to particle scattering on our simulations (which only introduces higher-order corrections), but multi-dimensional simulations are needed to further examine its impact. Especially, the resulting oblique magnetosonic modes would enhance the mirror effect as another important mechanism for scattering particles across the 90° pitch angle barrier (Felice & Kulsrud 2001; Holcomb & Spitkovsky 2019).

4.3. CR scattering

The main goal of this work is to provide self-consistent measurements of the CR scattering rates from our first-principle simulations, and here we lay out the procedures.

4.3.1. Pitch angle distribution

In Figure 6, we show in the left panel the pitch angle distribution at four representative particle momenta, taken from the fiducial run. This result can be interpreted from the wave-frame Fokker-Planck equation discussed in Section 3.2. In particular, the right-hand-

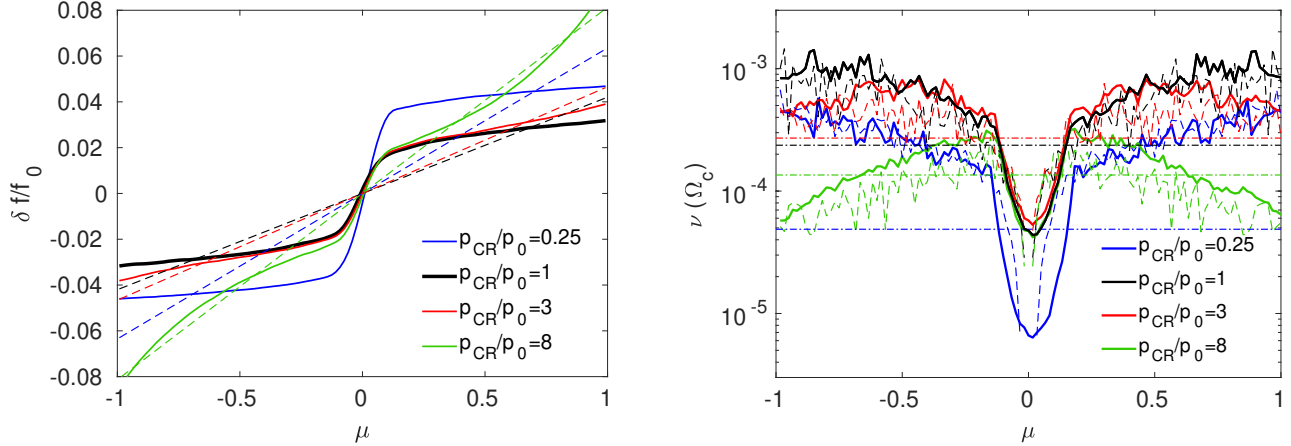


Figure 6. Left: deviation of the particle distribution function $f(p, \mu)$ from $f_0(p)$, shown at given $p = 0.25p_0, p_0, 3p_0$ and $8p_0$ (with different colors) as a function of pitch angle cosine μ . The corresponding dashed lines are line fits under the Eddington approximation (25). Right: the solid lines show the resulting total CR scattering rate obtained from Equation (20) for particles with the same momenta shown on the left. The dashed lines show the expected scattering rates based on QLD, given in Equation (19). The horizontal dash-dotted lines indicate the effective scattering rate for particles of the given momenta, given by Equation (28).

side of Equation (20) is independent of μ , which can be directly evaluated at the center of our simulation box. Therefore, the slope of $d\delta f/d\mu$ is inversely proportional to the pitch angle scattering rate $\nu(p, \mu)$, and it also reflects the level of isotropization at given μ .

For these particles with representative momenta, full isotropization in the wave frame is never achieved. For particles with $p \lesssim 3p_0$, the DF is close to isotropic (i.e., curve close to being flat) when μ is away from 0, indicating efficient scattering, but develops a steep slope around $\mu = 0$. This is a manifestation of the well-known $\mu = 0$ barrier, or 90° pitch angle barrier, where QLT fails. The fact that the slope is not infinite indicates that non-linear effects contribute to scattering. In fact, we have analyzed individual particle trajectories to examine the source of nonlinearity, and the results are very similar to BOPS19 (and hence not shown here), where reflections are generally found to be associated with particles entering the rotational discontinuities, a manifestation of non-linear wave-particle interaction. For particles with $p = 8p_0$, the fall-off of low- k modes makes their isotropization less efficient, leading to an increase of the $df/d\mu$ slope towards $|\mu| = 1$, whereas the slope near $\mu = 0$ remains similar to that for lower-energy particles.

We further examine the validity of the Eddington approximation (25), which essentially corresponds to fitting the $f(p, \mu)$ curve as a function of μ by a straight line. The results are shown as dashed lines in the left panel of Figure 6 for each momentum. Generally, we see substantial deviations near $\mu = 0$ because of the steepening of the $df/d\mu$ slope. Such deviations undermine the accuracy of this approximation. In particu-

lar, from Equations (23) and (31), the effective scattering rate is weighted by the $df/d\mu$ slope, and hence the less-isotropized $\mu \approx 0$ region carries a factor of a few more weight, a fact that was also noted in Bambi et al. (2021). As this region is characterized by smaller scattering rates, we thus anticipate the overall effective scattering rates to be smaller than those obtained by assuming Eddington approximation.

4.3.2. Primitive scattering rates

In the right panel of Figure 6, we show the inferred full scattering rates $\nu(p, \mu)$ from Equation (20). For comparison, we also show the expected scattering rate from QLD (19). We note that in computing these quantities, the derivative $df/d\mu$, as well as the raw wave energy spectrum, can be very noisy. We employ a Savitzky-Golay filter of with $n_L = n_R = 6$, $M = 2$, applied to both $f(p, \mu)$ and $I(k)$, to help mitigate the noise (which is also applied to obtain the right panel of Figure 5).

Generally, for particles with $p \lesssim 3p_0$, we find good agreement between the derived $\nu_\mu(p, \mu)$ and $\nu_{QL}(p, \mu)$ when μ is away from 0. This is consistent with that obtained in BOPS19, where detailed comparison between QLD and particle pitch angle evolution was carried out. At $\mu \approx 0$, on the other hand, we see that scattering rate from the QLD falls towards 0, whereas $\nu(p, \mu)$ remains finite, thanks to contributions from non-linear effects that assist the particles overcoming the $\mu = 0$ barrier.

For particles with $p = 8p_0$, we find our derived $\nu_\mu(p, \mu)$ is slightly higher than predicted from QLD. We have further examined particles with higher momentum, and find that deviation gradually increases. The underlying

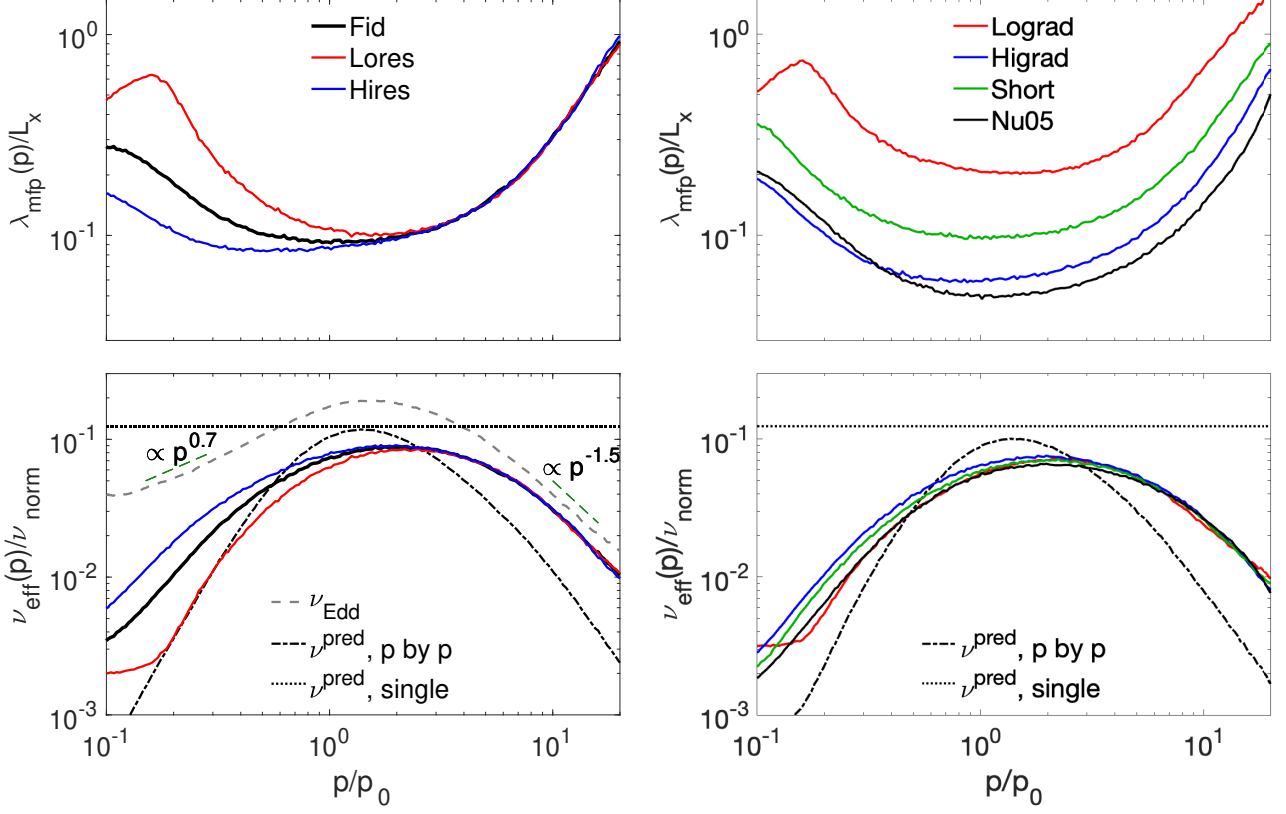


Figure 7. The effective scattering rate $\nu_{\text{sca}}(p)$ normalized by ν_{norm} (bottom), and the particle mean free path $\lambda_{\text{mfp}}(p)$ normalized by simulation box size L_x (top), shown as a function of momentum. Results are compared for runs with different resolutions (left) and with different CR pressure gradient and ion-neutral damping rate (right). In the bottom panels, we further show the theoretical scattering rates based on momentum-by-momentum treatment (46) in dash-dotted lines, as well as from single-fluid treatment (41) in horizontal dotted lines. Also shown in dashed line in the bottom left panel are the scattering rates expected from the Eddington approximation (26) based on our measured wave spectrum.

reason is that these particles are not sufficiently strongly scattered with a mean free path λ_{mfp} not small compared to simulation box size L_x (see Figure 7 and Section 5.1). Our simulation time is not yet long-enough to fully relax the spatial gradients, leading to an overestimate of $\partial P_{\text{CR}}/\partial x$.⁹ Nevertheless, the deviation is within a factor of two for $p \lesssim 10p_0$ and the effect on the overall momentum-integrated fluid scattering rate (to be discussed in Section 5.2) is very minor.

Integrating over μ , or from Equation (28), we further show in horizontal dash-dotted lines the value of $\nu_{\text{sca}}(p)$ at individual momentum p . This value is self-consistently measured from F_0 and F_1 , reflecting the aforementioned weighted average in Equations (23) and

(31). We can see by eye that the level indicated by ν_{sca} is lower compared to a simple average over the curve, and this is the most obvious for low-energy particles ($p \lesssim p_0$), highlighting the importance of kinetic simulations capturing the physics of CR scattering near $\mu = 0$.

While not shown here, we have also tracked the trajectories of a small fraction of particles to directly evaluate $D_{\mu\mu}$ defined in (18). The results are also in general agreement with our measured results. We note that similar agreement has been found in Bambi et al. (2021).

5. SIMULATION RESULTS: FLUID SCATTERING RATES FROM ALL RUNS

In this section, we compile data from all simulations and evaluate the momentum-by-momentum fluid scattering rate $\nu_{\text{sca}}(p)$ from Equation (28), from which we can also obtain particle mean free path $\lambda(p)$. The results are shown in Figure 7, with $\nu_{\text{sca}}(p)$ normalized by ν_{norm} (37), and λ_{mfp} normalized by L_x . For comparison, we also show the predicted scattering rates in dotted and dash-dotted lines for single-fluid and momentum-

⁹ Consider the case without scattering, one would eventually arrive at $\partial P_{\text{CR}}/\partial x = 0$. However, as we imposed a non-zero $\partial P_{\text{CR}}/\partial x$ at $t = 0$, reducing the gradient to zero would require all initial particles to traverse the box. For particles with pitch angles near $\mu = 0$, this would take many times L_x/C , which is well beyond our simulation time.

by-momentum treatments. The total fluid scattering rate ν_{sca} is then obtained by a weighted average of $\nu_{\text{sca}}(p)$ over momentum with $0.1p_0 < p < 10p_0$, given by Equation (34). Major diagnostic quantities associated with all simulation runs are also listed in Table 1, including the wave amplitudes E_{wave} , L_{CR} at the simulation box center, and the fluid scattering rate coefficient α_{sca} .

5.1. Scattering rates and mean free path by momentum

As a function of momentum, we see from the bottom left panel of Figure 7 that $\nu_{\text{sca}}(p)$ is maximized around $p \sim p_0 - 4p_0$, and falls off on both ends. Simulations with different resolutions agree for $p \gtrsim 2p_0$. In the low- p end, higher resolution yields higher scattering rates, and convergence is reached between run Fid and Hires down to about $0.5p_0$. This is a consequence of higher resolution being capable of better resolving smaller scales from the $I(k) \sim k^{-q}$ spectrum.

In the low- p range, we notice from the highest resolution run that at $p \lesssim p_0$, a power-law is developed with $\nu_{\text{sca}} \propto p^{0.7}$. The slope of $-0.7 \approx -(q-1)$ for non-relativistic particles is in line with the scaling from the Eddington approximation (27). In fact, the expected scattering rate from the Eddington approximation (26) based on our measured wave spectrum, shown in dashed line for run Fid, just has a normalization factor ~ 2.5 times higher (as it does not account for inefficient scattering across the $\mu = 0$ barrier). Therefore, even without reaching full convergence down to small p , we can well predict the converged behavior, and results from highest resolution is in fact close to this expectation down to $\sim 0.3p_0$. On the other hand, the predicted $\nu_{\text{sca}}^{\text{pred}}(p)$ for $p \lesssim p_0$ has a very different slope $\propto p^3$, leading to substantial deviations in the low- p end. This is the direct consequence of the $I(k) \sim k^{-1.7}$ spectrum discussed in Section 4.2 that overcomes wave damping and hence is much harder than standard expectations.

In the high- p range, we find a power law of $\nu_{\text{sca}} \propto p^{-1.5}$ which is, surprisingly, in line with the predicted slope of $p^{1-2\kappa}$ even though the low- k wave spectrum relevant to the resonant scattering does not show an extended power law. On the other hand, due to the cutoff in low- k wave spectrum, we expect the scaling of $\nu_{\text{sca}}(p)$ with p to drop off beyond $p \sim 10p_0$, though it is not yet seen due to limited domain size and simulation time. Our measured scattering rates are higher than predicted by a modest factor of 2–3.

The top left panel of Figure 7 shows the particle mean free paths λ_{mfp} as a function of p . Given our simulation box size of $L_x = 10^7 d_i$, we see that $L_x \gtrsim 5\lambda_{\text{mfp}}$ for particles with $p \lesssim 6p_0$, ensuring enough scattering within

the simulation box to validate our streaming box setting. We note that despite of having ν_{sca} decrease with momentum for low-energy particles, their λ_{mfp} remains close to flat. This is because these particles are sub-relativistic, and the reduction of particle speed largely cancels the reduction of ν_{sca} (see Equation (28)). For more energetic, relativistic particles, on the other hand, their λ_{mfp} increases rapidly with p , associated with the reduction of $\nu_{\text{sca}}(p)$ in the high- p end.

We further examine the role of CR pressure gradient and ion-neutral damping rate in the right panels of Figure 7. Most features are similar to those in the fiducial run. Remarkably, the measured scattering rates for all these runs, when normalized by ν_{norm} , largely overlap with each other, and they deviate from the predicted scattering rate in the same way as discussed earlier for the fiducial run. This is strong indication that the physics of the CRSI is independent of these parameters that we have varied, as anticipated from QLT. We have also examined the wave spectrum and found that their shapes are all similar to that of the fiducial run in both the high- k and low- k ranges. Besides, the run with higher/lower CR pressure gradient or weaker/stronger damping rate shows a lower/higher k_{min} in proportion with the gradient, in line with the discussion in Section 4.2. For most runs, the particle mean free path for the bulk CR population is well within our simulation box size. The case of run Lograd with relatively small imposed CR pressure gradient is more marginal, but still guarantees $L_x \gtrsim 3\lambda_{\text{mfp}}$ for $0.4p_0 \lesssim p \lesssim 5p_0$.

Overall, the predicted scattering rate based on single-fluid treatment (41) is always higher than the measured growth rate by a factor of ~ 2 at the peak with more significant overestimates at other momenta. The momentum-by-momentum treatment (46) yields closer estimate near the peak, though it significantly underestimates the scattering rates at the low- p end, and it also underestimates the scattering rates at the high- p end by a factor of a few.

5.2. Total fluid scattering rates

Finally, we discuss the fluid scattering rate ν_{sca} , computed from a weighted average of $\nu_{\text{sca}}(p)$ over p given by Equation (34). The results are normalized by ν_{norm} , with dimensionless scattering coefficient α_{sca} measured from all runs shown in Figure 8. As particles with $p \lesssim 0.1p_0$ and $p \gtrsim 10p_0$ are not very effectively scattered due to the lack of resolution (low- p) and finite box size and simulation time (high- p), we report the main results obtained by integrating over $0.1p_0 \leq p \leq p_0$ (in red filled circles). For comparison, we also show results obtained by integrating over the full range of p (in black

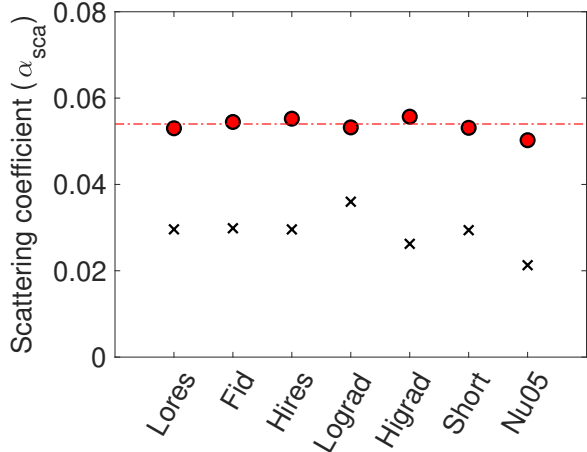


Figure 8. Measured dimensionless fluid scattering rates from all our simulation runs, normalized by ν_{norm} given by (37). Red filled circles correspond to results obtained by integrating over finite momentum range $0.1p_0 \leq p \leq 10p_0$, and black crosses correspond to those integrated over full range.

crosses). In the measurements, we use the value of L_{CR} measured directly from the simulations, given in Table 1. We note that the values of L_{CR} typically deviate from $(n_{\text{CR}}^{\text{cr}}/\Delta n_{\text{CR}})L_x$ by about $\lesssim 10\%$ (except for run Lograd where deviation is 18%). This correction is important given the level of precision in our measurements.

Remarkably, the numerical coefficients from all runs, regardless of the imposed pressure gradients and damping rates, agree very well with each other. Given the same resolution, runs with CR pressure gradient varied by more than a factor of 4 yield values that differ by no more than 5%. This result firmly establishes the scaling anticipated from QLT, and our work provides the accurately calibrated scattering coefficient. For particles with $0.1p_0 \leq p \leq 10p_0$, we find

$$\nu_{\text{sca}} \approx 0.054\nu_{\text{norm}}. \quad (48)$$

If we consider the full range of particle momenta, as shown in black crosses in Figure 8, we see that the coefficient α_{sca} is further lowered by a factor of ~ 2 to $\alpha_{\text{sca}} \sim 0.03$. The lowered values are almost entirely due to particles with momenta $p > 10p_0$ that we do not well accommodate. In Section 4.3.2, we have discussed that for such particles, due to limited simulation time, our estimates of $\nu_{\text{sca}}(p)$ is higher than the true value by a factor of $\gtrsim 2$. Therefore, if we extend p_{max} to $100p_0$, we expect the true value of α_{sca} to be even smaller, which we may quote $\alpha_{\text{sca}} \approx 0.01 - 0.02$ as the final scattering coefficient inferred from our simulations.

The coefficient $\alpha_{\text{sca}} \approx 0.054$ or $0.01 - 0.02$, is smaller by a factor of $\sim 2.5 - 10$ compared to our predicted value

of ~ 0.124 when treating CRs as a single fluid. This reduction is mainly due to the reduction of $\nu_{\text{sca}}(p)$ (thus enhancement of ν_s^{eff}) compared to the Eddington approximation, and accurate weighting from the momentum integral. On the other hand, our measured α_{sca} coefficient is comparable to the value of 0.046 or 0.0064, obtained from a momentum-by-momentum treatment mentioned at the end of Section 3.5.2. This agreement reflects some lucky cancellations: the predicted scattering rate is higher at the peak momentum, but lower at the low- p and high- p ends. For practical purposes, it is encouraging and suggests that Equations (46) and (47) are a viable prescription of CR scattering rates for $p \gtrsim p_0$.

6. DISCUSSION

6.1. Comparison to previous kinetic simulations

As a first kinetic study of the CRSI with driving thanks to the streaming box framework, our results can be compared with previous kinetic simulations with periodic boundary conditions (e.g., Bai et al. 2019; Holcomb & Spitkovsky 2019; Plotnikov et al. 2021). These simulations rely on a pre-existing CR streaming speed to excite the instability, and die out as the free-energy from initial CR streaming is exhausted. Usually, a large initial streaming speed or large CR number density drives waves to larger amplitudes, and facilitates particles crossing the $\mu = 0$ barrier, leading to full isotropization in the wave frame. On the other hand, with (more-realistic) low wave amplitudes, particles are isotropized separately for $\mu > 0$ and $\mu < 0$ regions, with a discontinuous jump at $\mu = 0$ owing to the 90° barrier, and the system reaches pre-matured saturation without full isotropization. We see from our new simulations that in the presence of background CR pressure gradient mimicking more realistic situations, the effective CR streaming speed is determined and maintained self-consistently, and by balancing growth with damping, steady wave amplitudes are achieved to allow CRs to develop a steady DF. We see that CRs are neither fully isotropized in the wave frame (which would reduce streaming speed in wave frame to zero), nor get stuck at $\mu = 0$ (the DF is steepened but without discontinuous jump at $\mu = 0$).

Even in a periodic box, a CR pressure gradient can be achieved by introducing an artificial interface separating regions with and without damping, thus breaking the translational symmetry. This approach allows Bambic et al. (2021) to make an attempt to compare kinetic simulation results to fluid theory over a transient phase, finding good agreement. Because the simulations are also powered by initial CR streaming, the comparison

with CR fluid theory includes a time-dependent term which accounts for the reduction of CR streaming over time. It could serve as a first step towards kinetic studies of multi-phase media, and we anticipate that our streaming box framework can also be extended to such studies to allow for a steady-state characterization of CR propagation in multi-phase media.

6.2. Implications for CR magnetohydrodynamics

A major goal of our study is to provide self-consistent scattering coefficients as sub-grid models for CR-MHD. While the CRs in CR-MHD would be dynamically-evolving, the steady state achieved in our kinetic simulations are valid and well justified to apply because of the dramatic separation between kinetic and fluid scales. The timescale for fluid environment to vary is expected to be on the order of L_{CR}/v_A , and the timescale for CR response is $\sim \nu_{\text{sca}}^{-1}$. Using (48), the ratio of the two is given by $L_{\text{CR}}\nu_{\text{sca}}/(v_A) \approx 0.03(n_{\text{CR}}/n_i)(c/v_A)^2(\Omega_c/\nu_{\text{in}})$, which is about 3×10^3 in our simulations. In more realistic environment, while there are multiple factors contributing, we anticipate $(n_{\text{CR}}/n_i)(c/v_A)^2 \sim$ order unity in typical Galactic ISM conditions, and ν_{in} being orders of magnitude lower than Ω_c , thus we expect the ratio to be $\gg 1$ in general, justifying the required scale-separation.

So far, most studies of CR hydrodynamics and CR transport adopt simple prescriptions of CR scattering rates or CR diffusivity, mostly as a constant. Very recently, more realistic prescriptions of CR transport are starting to be employed, based on QLT estimates (Hopkins et al. 2021b; Armillotta et al. 2021). Our momentum-by-momentum formula (45) is largely identical to that adopted by Armillotta et al. (2021), except for the minor difference where we explicitly treat the $\epsilon_{\text{CR}}/(\epsilon_{\text{CR}} + P_{\text{CR}})$ factor to be $3\mathcal{C}^2/(3\mathcal{C}^2 + v(p)^2)$ as opposed to their 3/4 assuming $v = c$. Therefore, the pros and cons discussed in Section 5 well applies to their work. Although Hopkins et al. (2021b) did not consider ion-neutral damping, their approach is very similar to our single-fluid treatment of CRs, and by the same token, we anticipate their adopted CR scattering rates can be a factor of $\gtrsim 10$ higher than realistic values if they were to include ion-neutral damping. It is yet to examine how much the results change when incorporating non-linear damping mechanisms such as non-linear Landau damping. In particular, as noted earlier, QLT is barely utilized in our derivations of the predicted scattering rates for the linear ion-neutral damping, and one may expect further deviations given the additional uncertainties in QLT when considering non-linear damping mechanisms.

We note that Hopkins et al. (2021b) calls for reduced CR scattering rates compared to QLT estimates by a factor of ~ 100 to match the integrated scattering rates for the Milky Way. Despite the dominant damping mechanisms in their simulations are not ion-neutral damping, our results of scattering rate reduction may account for a major fraction of the desired reduction. On the other hand, by post-processing very high resolution local simulations that well resolve the ISM, Armillotta et al. (2021) concluded there is no single CR diffusivity. Overall, the consequences of reduced scattering rate compared to those derived from conventional QLT remain to be seen, but we anticipate the resolution of a major uncertainty in the prescription will facilitate future studies to incorporate more realistic CR physics.

6.3. Implications for CR transport

The momentum-dependent CR scattering rates obtained from our simulations provide important calibrations for understanding CR transport in the self-confinement regime. Spectral breaks in Galactic CRs at rigidity $R \sim 200\text{GeV}$ have been interpreted as evidence for CR transport transitioning from being dominated by self-generated waves to extrinsic turbulence (Blasi et al. 2012; Evoli et al. 2018)¹⁰. Incorporating a well-calibrated CR scattering rate is thus crucial to accurately model CR transport for CR energies of $\lesssim 200\text{GeV}$, which also the energy range that plays a dominant role in CR feedback. Recently, it has also become possible to evolve a spectrum of CRs together with MHD (Girichidis et al. 2020; Hopkins et al. 2022a). Applications of this method to study CR-driven galactic wind have revealed rich physics and phenomenology, although the studies so far still assumed constant or phenomenological CR diffusion coefficients (Girichidis et al. 2021; Hopkins et al. 2022a). We anticipate that our calibrated prescriptions can lead to major improvements for better fidelity in future simulations.

In the meantime, we note that the standard CR self-confinement models based on QLT has very recently been called into question, as they appear to fail to reproduce the observed CR spectral slopes and the spectra of secondary-to-primary CRs (e.g. the B/C ratio), and that self-confinement may be inherently unstable (Kempski & Quataert 2022; Hopkins et al. 2022b). Our simulation results, being consistent with the QLT scalings, do not directly resolve the issue. However, these

¹⁰ We note that their adopted wave growth rate, which can be derived by combining our Equations (43) and (45) and (crudely) substituting $\nu_{\text{sca}}(p)$ by $\pi\Omega k_{\text{res}}I(k_{\text{res}})$, is a factor ~ 4 larger than ours.

works have not necessarily exhausted all the possibly relevant physics, especially microphysics, and the nature of the multi-phase interstellar and circumgalactic medium always lead to further complications. Even though the streaming framework is subject to imposed CR densities at the two boundaries, it still offers certain freedom to conduct controlled experiments around the box center region (a few mean free paths away from the boundaries), and thus we anticipate it will become a powerful tool to further investigate the kinetic aspects of this dilemma.

Besides, low-energy CRs are important source of ionization, especially in high-density, weakly-ionized regions such as molecular clouds and protoplanetary disks, which determine how strong gas and magnetic fields couple, with significant dynamical consequences. There has been considerable recent research interest in studying the generation and propagation of CRs in these environments (see e.g., [Padovani et al. 2020](#) for a review). Penetration of CRs in molecular clouds ([Everett & Zweibel 2011](#); [Ivlev et al. 2018](#); [Silsbee & Ivlev 2019](#)) plays a significant role regulating star formation (e.g., [Zhao et al. 2020](#); [Semenov et al. 2021](#)). The ionization rate also crucially influences the gas dynamics of protoplanetary disks, where it is uncertain whether CRs are excluded by stellar and/or disk winds ([Cleeves et al. 2013](#)). It has also been proposed that young stellar objects themselves are sources of CRs ([Padovani et al. 2016](#)), which may significantly impact disk ionization ([Offner et al. 2019](#); [Rodgers-Lee et al. 2020](#)). Due to the largely unknown diffusion coefficients, empirical diffusion coefficients are exclusively used in model calculations. It is yet to examine whether and where self-generated waves can dominate CR scattering in such environments, thus helps elucidate and reduce dramatic uncertainties.

7. SUMMARY AND CONCLUSIONS

In this work, we have described a novel, multi-scale numerical framework, the streaming box, to simulate the driving of the CRSI at kinetic level and enable self-consistent measurement of the CR scattering rates. The streaming box can be considered as a local patch along magnetic fields in a global system, which is macroscopically short compared with system size, but microscopically long so as to contain multiple CR mean free paths. By imposing and maintaining a CR pressure gradient at box boundaries, the system develops a CR flux through the box that constantly drives the CRSI towards steady state, where wave growth is balanced by damping (here ion-neutral damping), realizing the classic scenario expected from QLT. This enables us to conduct detailed study to test CR fluid theory and measure the result-

ing CR transport coefficients as a function of system parameters.

We implemented this framework in the Athena code, using its MHD-PIC module. In doing so, we have devised a CR injection recipes at the box boundaries to sustain the CR gradient, and made it compatible with the δf weighting scheme which dramatically reduces the Poisson noise. We have also presented a theoretical framework for measuring scattering rates from the most primitive form, to the fluid scattering rate that is weighted average of the primitive rates. We also derived two versions of theoretically expected scattering rate based on QLT yet with substantially different predictions, reflecting the dramatic uncertainty and ambiguity in determining such coefficients in the literature.

We conducted a series of simulations with different resolutions and CR pressure gradients with ion-neutral damping, and our main findings are as follows.

- At saturated state, wave energy spectrum peaks around the resonant wavelength of particles with $p \sim p_0$ (characteristic momentum of the CR distribution). The high- k range develops into a power law wave energy spectrum with $I(k) \propto k^{-1.7}$ following a cascade, whereas the low- k part of the spectrum develops a different power-law ($\propto k^{0.15}$) before undergoing a cut-off due to wave damping.
- The CRs are not fully isotropized. Particles with momentum \lesssim a few p_0 are close to isotropization away from $\mu = 0$, followed by a more steep transition across $\mu = 0$. This challenges the validity of the Eddington approximation with modest reduction of the effective scattering rates. The Eddington approximation is better applicable to more energetic particles, though most of these particles are inefficiently scattered due to the cut-off of the low- k wave spectrum.
- The total fluid scattering rates, after integrating over momentum, conform to the scalings expected from QLT. In particular, the effective streaming speed is independent of imposed CR pressure gradient. Compared with theoretical expectations:
 - QLT based on single-fluid treatment of CRs underestimates the effective CR streaming speed by a factor of > 2 , leading to an overestimate of CR scattering rates by up to an order of magnitude.
 - QLT based on momentum-by-momentum treatment of CRs show reasonable agreement with our measurements when integrated over momentum near the peak of the distribution function, but

bears large uncertainties at individual momenta especially at low- p ends.

- When ion-neutral damping dominates, we recommend using (48) for single-fluid CR scattering rates with CR energy up to $p = 10p_0$, and (46) for momentum-dependent scattering rates with $p \gtrsim p_0$. A $\nu_{\text{sca}}(p) \propto p^{0.7}$ scaling is applicable in the low-momentum range.

Overall, we have provided the first numerical measurement of the CR scattering rates from first-principles for the bulk CR population subject to self-confinement, which bridges the gap between kinetic (CR-gyro) and fluid (λ_{mfp}) scales. We anticipate it will offer realistic sub-grid prescriptions for CR-MHD simulations at macroscopic scales for studies of CR transport and feedback, thus eliminating a major source of uncertainty in such simulations. This will help clarify the much unknown role played by the CRs on scales ranging from the local ISM to those at galactic scales or beyond.

As an initial study, we have limited ourselves to 1D and the simplest ion-neutral damping to demonstrate the utility of the streaming box framework. This framework is fully generalizable to multi-dimensions, which

can be important to investigate additional scattering mechanisms that are not captured in 1D. While some of the additional damping mechanisms, such as non-linear Landau damping, requires resolving the kinetic physics of background plasmas which are missing in our MHD treatment, such mechanisms can in principle be manually incorporated by operating in Fourier space. Therefore, we anticipate that our study opens up the window towards fully characterizing the CR scattering rates over a wide range of regimes, thus providing a comprehensive suite of sub-grid prescriptions for future CR-MHD simulations of CR transport and feedback.

- 1 I thank Eve Ostriker and Chris Bambic for helpful
- 2 discussions and comments to a preliminary version of
- 3 the draft, and the anonymous referee for a thoughtful
- 4 and constructive report. This research is supported by
- 5 the National Science Foundation of China under Grant
- 6 No. 11873033. Numerical simulations are conducted
- 7 on TianHe-1 (A) at National Supercomputer Center in
- 8 Tianjin, China, and on the Orion cluster at Department
- 9 of Astronomy, Tsinghua University.

REFERENCES

- Aloisio, R., Blasi, P., & Serpico, P. D. 2015, *A&A*, 583, A95
- Amato, E. & Blasi, P. 2018, *Advances in Space Research*, 62, 2731
- Armillotta, L., Ostriker, E. C., & Jiang, Y.-F. 2021, *ApJ*, 922, 11
- Bai, X.-N., Caprioli, D., Sironi, L., & Spitkovsky, A. 2015, *ApJ*, 809, 55
- Bai, X.-N., Ostriker, E. C., Plotnikov, I., & Stone, J. M. 2019, *ApJ*, 876, 60
- Bambic, C. J., Bai, X.-N., & Ostriker, E. C. 2021, *ApJ*, in press, arXiv:2102.11877
- Bell, A. R. 1978, *MNRAS*, 182, 147
- Birdsall, C. K. & Langdon, A. B. 2005, *Plasma Physics Via Computer Simulation* (Taylor & Francis Group, 2005)
- Blandford, R. D. & Ostriker, J. P. 1978, *ApJL*, 221, L29
- Blasi, P., Amato, E., & Serpico, P. D. 2012, *PhRvL*, 109, 061101
- Booth, C. M., Agertz, O., Kravtsov, A. V., & Gnedin, N. Y. 2013, *ApJL*, 777, L16
- Boris, J. P. 1970, in *Proceedings of the Fourth Conference on Numerical Simulation Plasmas* (Naval Research Laboratory, Washington, D.C.), pp. 3–67
- Breitschwerdt, D., McKenzie, J. F., & Voelk, H. J. 1991, *A&A*, 245, 79
- Chan, T. K., Kereš, D., Hopkins, P. F., Quataert, E., Su, K. Y., Hayward, C. C., & Faucher-Giguère, C. A. 2019, *MNRAS*, 488, 3716
- Cleeves, L. I., Adams, F. C., & Bergin, E. A. 2013, *ApJ*, 772, 5
- Cohen, R. H. & Kulsrud, R. M. 1974, *Physics of Fluids*, 17, 2215
- Denton, R. E. & Kotschenreuther, M. 1995, *Journal of Computational Physics*, 119, 283
- Dimits, A. M. & Lee, W. W. 1993, *Journal of Computational Physics*, 107, 309
- Drury, L. O. 1983, *Reports on Progress in Physics*, 46, 973
- Everett, J. E. & Zweibel, E. G. 2011, *ApJ*, 739, 60
- Everett, J. E., Zweibel, E. G., Benjamin, R. A., McCammon, D., Rocks, L., & Gallagher, III, J. S. 2008, *ApJ*, 674, 258
- Evoli, C., Blasi, P., Morlino, G., & Aloisio, R. 2018, *PhRvL*, 121, 021102
- Farmer, A. J. & Goldreich, P. 2004, *ApJ*, 604, 671
- Felice, G. M. & Kulsrud, R. M. 2001, *ApJ*, 553, 198
- Ferrière, K. M. 2001, *Reviews of Modern Physics*, 73, 1031
- Foote, E. A. & Kulsrud, R. M. 1979, *ApJ*, 233, 302
- Ginzburg, V. L. & Syrovatskii, S. I. 1964, *The Origin of Cosmic Rays* (New York: Macmillan)

- Girichidis, P., Naab, T., Walch, S., Hanasz, M., Mac Low, M.-M., Ostriker, J. P., Gatto, A., Peters, T., Wünsch, R., Glover, S. C. O., Klessen, R. S., Clark, P. C., & Baczynski, C. 2016, *ApJL*, 816, L19
- Girichidis, P., Pfrommer, C., Hanasz, M., & Naab, T. 2020, *MNRAS*, 491, 993
- Girichidis, P., Pfrommer, C., Pakmor, R., & Springel, V. 2021, arXiv e-prints, arXiv:2109.13250
- Grenier, I. A., Black, J. H., & Strong, A. W. 2015, *ARA&A*, 53, 199
- Guo, F. & Oh, S. P. 2008, *MNRAS*, 384, 251
- Hanasz, M., Lesch, H., Naab, T., Gawryszczak, A., Kowalik, K., & Wóltański, D. 2013, *ApJL*, 777, L38
- Hawley, J. F., Gammie, C. F., & Balbus, S. A. 1995, *ApJ*, 440, 742
- Holcomb, C. & Spitkovsky, A. 2019, *ApJ*, 882, 3
- Hopkins, P. F., Chan, T. K., Ji, S., Hummels, C. B., Kereš, D., Quataert, E., & Faucher-Giguère, C.-A. 2021a, *MNRAS*, 501, 3640
- Hopkins, P. F., Squire, J., Chan, T. K., Quataert, E., Ji, S., Kereš, D., & Faucher-Giguère, C.-A. 2021b, *MNRAS*, 501, 4184
- Hopkins, P. F., Butsky, I. S., Panopoulou, G. V., Ji, S., Quataert, E., Faucher-Giguère, C.-A., & Keres, D. 2022a, arXiv:2109.09762
- Hopkins, P. F., Squire, J., Butsky, I. S., et al. 2022, submitted to *MNRAS*, arXiv:2112.02153
- Hu, G. & Krommes, J. A. 1994, *Physics of Plasmas*, 1, 863
- Huang, X. & Davis, S. W. 2022, *MNRAS*doi:10.1093/mnras/stac059
- Ipavich, F. M. 1975, *ApJ*, 196, 107
- Ivlev, A. V., Dogiel, V. A., Chernyshov, D. O., Caselli, P., Ko, C. M., & Cheng, K. S. 2018, *ApJ*, 855, 23
- Ji, S. & Hopkins, P. F. 2021, arXiv e-prints, arXiv:2111.14704
- Jiang, Y.-F. & Oh, S. P. 2018, *ApJ*, 854, 5
- Jokipii, J. R. 1966, *ApJ*, 146, 480
- Kempski, P. & Quataert, E. 2022, submitted to *MNRAS*, arXiv:2109.10977
- Kulsrud, R. & Pearce, W. P. 1969, *ApJ*, 156, 445
- Kulsrud, R. M. & Cesarsky, C. J. 1971, *Astrophys. Lett.*, 8, 189
- Kunz, M. W., Stone, J. M., & Bai, X.-N. 2014, *Journal of Computational Physics*, 259, 154
- Lazarian, A. 2016, *ApJ*, 833, 131
- Lee, M. A. & Völk, H. J. 1973, *Ap&SS*, 24, 31
- Mao, S. A. & Ostriker, E. C. 2018, *ApJ*, 854, 89
- McKenzie, J. F. & Voelk, H. J. 1982, *A&A*, 116, 191
- Naab, T. & Ostriker, J. P. 2017, *ARA&A*, 55, 59
- Offner, S. S. R., Gaches, B. A. L., & Holdship, J. R. 2019, *ApJ*, 883, 121
- Padovani, M., Ivlev, A. V., Galli, D., Offner, S. S. R., Indriolo, N., Rodgers-Lee, D., Marcowith, A., Girichidis, P., Bykov, A. M., & Kruijssen, J. M. D. 2020, *SSRv*, 216, 29
- Padovani, M., Marcowith, A., Hennebelle, P., & Ferrière, K. 2016, *A&A*, 590, A8
- Pakmor, R., Pfrommer, C., Simpson, C. M., & Springel, V. 2016, *ApJL*, 824, L30
- Parker, S. E. & Lee, W. W. 1993, *Physics of Fluids B*, 5, 77
- Pfrommer, C., Pakmor, R., Schaal, K., Simpson, C. M., & Springel, V. 2017, *MNRAS*, 465, 4500
- Plotnikov, I., Ostriker, E. C., & Bai, X.-N. 2021, *ApJ*, 914, 3
- Quataert, E., Jiang, Y.-F., & Thompson, T. A. 2022, *MNRAS*, 510, 920
- Rodgers-Lee, D., Taylor, A. M., Downes, T. P., & Ray, T. P. 2020, *MNRAS*, 491, 4742
- Roe, P. L. 1981, *Journal of Computational Physics*, 43, 357
- Ruszkowski, M., Yang, H.-Y. K., & Zweibel, E. 2017, *ApJ*, 834, 208
- Salem, M. & Bryan, G. L. 2014, *MNRAS*, 437, 3312
- Schlickeiser, R. 2002, *Cosmic Ray Astrophysics* (Springer)
- Schlickeiser, R. & Miller, J. A. 1998, *ApJ*, 492, 352
- Semenov, V. A., Kravtsov, A. V., & Caprioli, D. 2021, *ApJ*, 910, 126
- Silsbee, K. & Ivlev, A. V. 2019, *ApJ*, 879, 14
- Simpson, C. M., Pakmor, R., Marinacci, F., Pfrommer, C., Springel, V., Glover, S. C. O., Clark, P. C., & Smith, R. J. 2016, *ApJL*, 827, L29
- Skilling, J. 1971, *ApJ*, 170, 265
- . 1975, *MNRAS*, 172, 557
- Soler, R., Terradas, J., Oliver, R., & Ballester, J. L. 2016, *A&A*, 592, A28
- Squire, J., Hopkins, P. F., Quataert, E., & Kempski, P. 2021, *MNRAS*, 502, 2630
- Stone, J. M., Gardiner, T. A., Teuben, P., Hawley, J. F., & Simon, J. B. 2008, *ApJS*, 178, 137
- Strong, A. W., Moskalenko, I. V., & Ptuskin, V. S. 2007, *Annual Review of Nuclear and Particle Science*, 57, 285
- Thomas, T. & Pfrommer, C. 2019, *MNRAS*, 485, 2977
- Thomas, T., Pfrommer, C., & Pakmor, R. 2021, *MNRAS*, 503, 2242
- Uhlig, M., Pfrommer, C., Sharma, M., Nath, B. B., Enflin, T. A., & Springel, V. 2012, *MNRAS*, 423, 2374
- Wentzel, D. G. 1974, *ARA&A*, 12, 71
- Wiener, J., Oh, S. P., & Guo, F. 2013, *MNRAS*, 434, 2209
- Wiener, J., Pfrommer, C., & Oh, S. P. 2017, *MNRAS*, 467, 906

- Wiener, J., Zweibel, E. G., & Oh, S. P. 2018, *MNRAS*, 473, 3095
- Yan, H. & Lazarian, A. 2002, *Physical Review Letters*, 89, 281102
- Zhao, B., Tomida, K., Hennebelle, P., Tobin, J. J., Maury, A., Hirota, T., Sánchez-Monge, Á., Kuiper, R., Rosen, A., Bhandare, A., Padovani, M., & Lee, Y.-N. 2020, *SSRv*, 216, 43
- Zirakashvili, V. N., Breitschwerdt, D., Ptuskin, V. S., & Voelk, H. J. 1996, *A&A*, 311, 113
- Zweibel, E. G. 2017, *Physics of Plasmas*, 24, 055402

APPENDIX

A. THE STREAMING BOX IMPLEMENTATION

A.1. *The Injection Boundary Condition*

The key in implementing the streaming box is the CR injection boundary condition. We first note that the DF of particles *entering the box from the boundary* (i.e. for the CR flux) differs from DF at the boundary, because particles traveling faster along \hat{x} direction have higher probability to be injected. While it is possible to work out the new DF, it is not necessarily analytic and requires additional effort for numerical implementation. Instead, we adopt a much simpler injection recipes that mimics the real flow of particles and does not require calculating the DF for CR flux.

Suppose we aim to set up N particles per cell for a CR number density $n_{\text{CR}}^{\text{ctr}}$. At the two boundaries, the desired CR number densities are $n_{\text{CR}}^{\text{hi}}$ and $n_{\text{CR}}^{\text{lo}}$ respectively. Let Δx be the cell size, which is uniform, and Δt be simulation timestep. Over time Δt , the particles can at most travel over a distance of $\Delta L = \mathbb{C}\Delta t$, which is typically comparable to Δx . We define

$$N' = \text{ceil}\left(\frac{\Delta L}{\Delta x} N \frac{n_{\text{CR}}^X}{n_{\text{CR}}^{\text{ctr}}}\right), \quad \Delta L' = \frac{N'}{N} \frac{n_{\text{CR}}^{\text{ctr}}}{n_{\text{CR}}^X} \Delta x, \quad (\text{A1})$$

where the $\text{ceil}(y)$ function takes the smallest integer that is larger than y , and superscript ‘ X ’ denotes either “lo” or “hi”.

In each simulation timestep, we will randomly inject N' particles over a distance of $\Delta L'$ just *outside* of the left/right boundary, with each particle k assigned a random location x_k , and a random momentum vector following the desired DF at the boundary. After time Δt , these particles would end up at position $x'_k = x_k + v_{kx}\Delta t$. We only keep the particles whose new positions x'_k are *inside* the simulation domain, while other particles are deleted.

A.2. *The δf weighting scheme*

When the CR DF $f(\mathbf{x}, \mathbf{p})$ is close to some steady background DF $f_0(\mathbf{x}, \mathbf{p})$ that is known, one can take this advantage and consider individual particles as Lagrangian markers representing the difference, δf , between f and f_0 (instead of f). This is handled by a weighting scheme known as the δf method (Parker & Lee 1993; Dimits & Lee 1993; Hu & Krommes 1994; Denton & Kotschenreuther 1995; Kunz et al. 2014), as opposed to the “full- f ” scheme. This δf weighting scheme has been implemented to our MHD-PIC code in BOPS19, which dramatically beats down Poisson noise and proves to be indispensable to accurately follow wave growth and quasi-linear evolution of particles.

The δf scheme is based on the Liouville theorem: the DF f is constant along particle trajectories in phase space. As described in BOPS19, we record the initial value of f at $t = 0$ (i.e., f_0) for all particles, and then at every time t , a weight w_j is assigned to each particle j as

$$w_j \equiv \frac{\delta f(t, \mathbf{x}_j(t), \mathbf{p}_j(t))}{f(t, \mathbf{x}_j(t), \mathbf{p}_j(t))} = 1 - \frac{f_0(\mathbf{x}_j(t), \mathbf{p}_j(t))}{f_0(\mathbf{x}_j(0), \mathbf{p}_j(0))}. \quad (\text{A2})$$

The CR number density and current density can then be obtained by

$$\begin{aligned} \begin{bmatrix} n_{\text{CR}}(t, \mathbf{x}) \\ \mathbf{J}_{\text{CR}}(t, \mathbf{x}) \end{bmatrix} &= \begin{bmatrix} n_{\text{CR},0}(\mathbf{x}) \\ \mathbf{J}_{\text{CR},0}(\mathbf{x}) \end{bmatrix} + \int \begin{bmatrix} 1 \\ q\mathbf{v}(\mathbf{p}) \end{bmatrix} \delta f(t, \mathbf{x}, \mathbf{p}) d^3\mathbf{p} \\ &\simeq \begin{bmatrix} n_{\text{CR},0}(\mathbf{x}) \\ \mathbf{J}_{\text{CR},0}(\mathbf{x}) \end{bmatrix} + \sum_{j=1}^{N_p} w_j \begin{bmatrix} 1 \\ q\mathbf{v}_j \end{bmatrix} S(\mathbf{x} - \mathbf{x}_j), \end{aligned} \quad (\text{A3})$$

where $S(\mathbf{x})$ is the shape function corresponding to the TSC interpolation scheme, and $n_{\text{CR},0}$ and $\mathbf{J}_{\text{CR},0}$ are obtained directly from f_0 . Note that the conventional full- f scheme corresponds to setting $w_j = 1$, $n_{\text{CR},0} = 0$ and $\mathbf{J}_{\text{CR},0} = 0$.

In the streaming box framework, by requiring $\Delta n_{\text{CR}}/n_{\text{CR}}^{\text{ctr}} \ll 1$, it follows that the variation of the CR DF across the box is on the same order. Therefore, the advantage of the δf weighting scheme is naturally preserved. The remaining question is, how should we choose the background DF $f_0(\mathbf{x}, \mathbf{p})$? We note that f_0 does not necessarily be an equilibrium DF, leaving us some freedom to choose it properly for our convenience, and we can envisage two cases.

- Case I, suppose CRs are sufficiently scattered so that upon saturation, the system approaches a quasi-isotropic state with a gradient in accordance with the imposed CR density gradient. This will yield a background DF to be

$$f_0^I(x, p) = \frac{n_{\text{CR},0}(x)}{n_{\text{CR}}^{\text{ctr}}} f_0^{\text{ctr}}(p), \quad (\text{A4})$$

where $f_0^{\text{ctr}}(p)$ is the mean background (isotropic) DF (or the desired DF at box center).

- Case II, consider the opposite limit, where there is no scattering and all CR particles travel through the box unimpeded. Due to the different CR number density (and hence flux) imposed at the two boundaries, there is an asymmetry/discontinuity in the overall CR DF

$$f_0^{\text{II}}(x, p, \mu) = \begin{cases} [n_{\text{CR}}^{\text{hi}}/n_{\text{CR}}^{\text{ctr}}] f_0^{\text{ctr}}(p) & (\mu > 0) \\ [n_{\text{CR}}^{\text{lo}}/n_{\text{CR}}^{\text{ctr}}] f_0^{\text{ctr}}(p) & (\mu < 0) \end{cases}, \quad (\text{A5})$$

where $\mu \equiv \cos \theta$ is the cosine of particle pitch angle (in wave frame, by default), with $\mu > 0$ representing forward traveling CRs.

We have experimented both approaches and they yield similar results. In practice, we choose case I for two reasons. First, our desired saturated state does require sufficient scattering in the simulation box thus the final CR DF is closer to (A4). Second, the initial DF from case I allows the instability to develop faster. This is because in case I, CR anisotropy can quickly build up at initial stage (in the absence of initial perturbation) to drive the CRSI. In case II, however, most of the initial anisotropy lies in the discontinuity across 90° pitch angle, which generally requires finite-amplitude initial perturbations (which we do not prefer) to “release” its free energy.

A.3. Choice of frames

In the streaming box framework, additional degrees of freedom arise from the choice of frames. This choice is two-fold. The first is about the background gas velocity v_{g0} (which is uniform by construction), and the second is related to particle injection, as one can apply a certain velocity boost $v_{\text{CR},d}$ to all injected particles.

With periodic boundary conditions for the background gas, different choices of frames are essentially equivalent. However, we have found that it would be particularly beneficial to adopt the Alfvén wave frame, primarily for numerical reasons: we find that numerical damping of Alfvén waves is much weaker if the simulation is conducted in the wave frame. This is helpful given that our simulations must cover a wide range of scales and by working in the wave frame it leads to effectively higher resolution and hence saves some computational cost. Therefore, we choose to adopt the wave-frame as a first study.

Once the frame for background gas is settled, choices of different frames for particles are not equivalent. However, as long as $L \gg \lambda_{\text{mfp}}$ and $v_{g0}, v_{\text{CR},d} \ll \mathbb{C}$, we anticipate that the CRs should be sufficiently scattered to establish the desired steady state away from the boundaries. We note that this state must have certain level of anisotropy as CRs diffuse/stream downward the pressure gradient, which is a main product of our simulation that we cannot know *a priori*. This means that it is virtually impossible to set the frame of CR injection that perfectly matches the final level of anisotropy. Therefore, we simply assume zero drift velocity, and inject CRs isotropically at the boundaries, followed by the injection recipes that we just described.

Because of a small level of mismatch between the injection frame and the frame of CR streaming in saturated state, there must be a relaxation zone near the boundaries through which a transition occurs, whose thickness is on the order of λ_{mfp} . Therefore, we always conduct measurement near the center of the simulation box, which is free from boundary artifacts. We also caution that the CR density/pressure gradient in the central region of the box does not necessarily be equal to the mean density/pressure gradient that we impose, but has small deviations due to the boundary relaxation zone. We therefore report results based on the true CR density/pressure gradients measured in the central region of our simulation box, together with the actual value of L_{CR} measured in this region.

B. ESTIMATING THE CR PITCH ANGLE SCATTERING RATE

Here we derive Equation (20) from Equation (17), under the steady state assumption. In this case, we have

$$\mu V(p) \frac{\partial f}{\partial x} = \frac{\partial}{\partial \mu} \left(\frac{1 - \mu^2}{2} \nu_\mu(p, \mu) \frac{\partial f}{\partial \mu} \right). \quad (\text{B6})$$

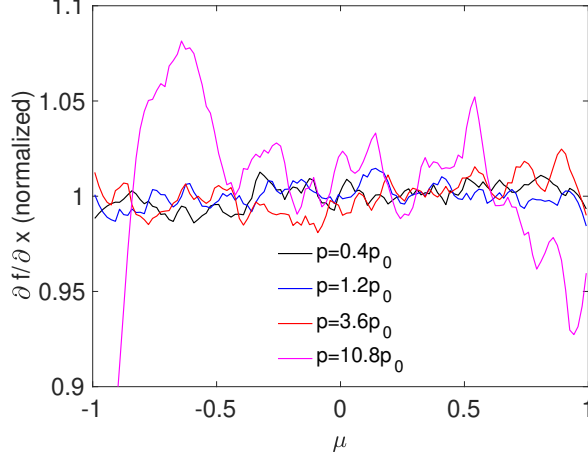


Figure 9. Spatial gradient $\partial f/\partial x$ as a function of μ for different momentum bins as indicated in the legend. The gradient is normalized by $\partial \bar{f}/\partial x$ where \bar{f} is f averaged over μ . The lines are largely flat as long as steady state is achieved.

First of all, we can easily verify that if $\partial f/\partial x$ is independent of μ , then Equation (20) is the exact solution to this equation. As long as f does not strongly deviate from f_0 , we should anticipate $\partial f/\partial x \approx \partial f_0/\partial x$, with the latter being independent of μ . Therefore, we expect Equation (20) to hold at least approximately. That is, $\nu_\mu \partial f/\partial \mu$ should be largely independent of μ . More rigorously, noticing that both ν_μ and $\partial f/\partial \mu$ should be even functions of μ by symmetry, we may expand it as

$$\nu_\mu \frac{\partial f}{\partial \mu} \approx A_0 + \mu^2 A_1 + \mu^4 A_2 + \dots, \quad (\text{B7})$$

with $A_2 \ll A_1 \ll A_0$, etc. Applying this expansion to (B6), we obtain

$$V(p) \frac{\partial f}{\partial x} \approx -(A_0 - A_1) - 2\mu^2(A_1 - A_2) + O(\mu^4). \quad (\text{B8})$$

This suggests that $\partial f/\partial x$ must be an even function of μ as well, which we may write as $\partial f/\partial x \approx B_0 + B_1\mu^2 + \dots$. By matching the terms of the same order, we see that the error in estimating ν_μ from Equation (20) is about $\delta\nu_\mu/\nu_\mu \sim A_1/A_0 \sim B_1/B_0$.

In Figure 9, we show the ratio of $\partial f/\partial x$ over $\partial \bar{f}/\partial x$, where \bar{f} is the μ -averaged DF for different particle momenta in our run Fid. It is clear that for particle momenta $p \lesssim 5p_0$, the dependence of $\partial f/\partial x$ on μ is almost indistinguishable from being flat, which we estimate $B_1/B_0 < 1\%$. We already noted that particles with $p \gtrsim 10p_0$ has not yet reached steady state, thus it is conceivable that $\partial f/\partial x$ at these momentum bins show more substantial deviations. Overall, the results justify the precision of Equation (20) in estimating the primitive CR pitch angle scattering rate $\nu_\mu(p, \mu)$.

C. CR MOMENTUM FEEDBACK AND CR HEATING

As a by-product, the streaming CRs provide momentum and energy feedback to background gas. Momentum feedback is achieved by momentum exchange between CRs and waves, whose net effect pushes gas in the direction of CR streaming. Energy feedback is due to wave damping which heats up the gas, balanced by wave growth driven by the CRSI. This process is better known as CR heating.

The discussion on the energetics is most convenient in the wave frame, as in our simulations. From a fluid perspective, momentum conservation is exhibited as Equation (31), where the right hand side reflects the backreaction to background gas $G(p)$:

$$G(p) \equiv \frac{\nu_{\text{sca}}(p)\mathcal{F}_{\text{CR}}}{\mathbb{C}^2} = \frac{4\pi p^3 v(p)E(p)}{\mathbb{C}^2} \int_{-1}^1 \frac{\partial f}{\partial \mu} \frac{1-\mu^2}{4} \nu(p, \mu) d\mu, \quad (\text{C9})$$

and total CR force is given by $\int G(p) d \ln p$.

In the wave frame, there is no energy exchange between the CRs and background gas. Therefore, growth of wave energy is compensated by reduction of the kinetic energy of the gas, which can be considered as the work done by

$\int G(p)d\ln p$. In steady state, this is balanced by energy dissipation through wave damping (“CR heating”), and we have

$$\Gamma_{\text{heat}} = v_A \int G(p)d\ln p = \nu_{\text{in}} \langle \rho \delta v^2 \rangle \approx \nu_{\text{in}} \rho v_A^2 \int I(k)dk = \nu_{\text{in}} \rho v_A^2 E_{\text{wave}} , \quad (\text{C10})$$

where angle bracket represents spatial average, and we have taken $\rho \delta v^2 \approx \delta B^2$ for Alfvén waves.

In the parallel direction, the development of the CRSI accelerates background ions relative to the neutrals, while ion-neutral drag keeps the ions and neutrals at similar speed. Balancing acceleration with drag, we have

$$\int G(p)d\ln p = \nu_{\text{in}} \rho \Delta v_g , \quad (\text{C11})$$

where $\Delta v_g = v_g - v_{g0}$ is the velocity difference between background ions and neutrals. Comparing the above two equations, we obtain

$$\Delta v_g = v_A E_{\text{wave}} . \quad (\text{C12})$$

Therefore, the gas velocity v_g will slightly deviate from our intended velocity of $-v_A$ (so that the simulation is conducted in the wave frame). Nevertheless, as long as $\Delta v_g \ll v_A$, or $\delta B^2 \ll B_0^2$ (in our simulations on the order of 1% or less), the deviation is largely negligible. In Table 1, we can see that given $v_A = 1$, Δv_g and E_{wave} are largely identical within 1% – 5%, thus confirming the energetics between momentum feedback and CR heating. Moreover, in the fiducial simulation, the heating rate is about $2.7 \times 10^{-7} \Omega_c^{-1}$ in code units, which can at most contribute to increase temperature by $\lesssim 6\%$ over the course of our simulation. The long heating timescale provides another justification for our use of isothermal equation of state.

One final piece of verification, as $G(p)$ is balanced by the of CR pressure gradient from Equation (31), we thus anticipate

$$\int G(p)d\ln p = \left| \frac{\partial P_{\text{CR}}}{\partial x} \right| \approx \frac{P_{\text{CR}}^{\text{ctr}}}{L_{\text{CR}}} \approx \nu_{\text{in}} \rho \Delta v_g \approx \nu_{\text{in}} \rho v_A E_{\text{wave}} . \quad (\text{C13})$$

For the fiducial run, we find $|\partial P_{\text{CR}}/\partial x|$, integrated over the entire particle population, to be $\sim 3.04 \times 10^{-7}$ in code units, higher than the expected value of $\sim 2.7 \times 10^{-7}$. As we discussed in Section 4.3.2, for particles with $p \lesssim 0.1p_0$ and $p \gtrsim 10p_0$, steady state is not quite achieved due to the inefficient scattering (long mean free paths) and insufficient simulation time for all particles to traverse the simulation box. Therefore, the gradient of P_{CR} integrated over these momenta is not fully compensated by scattering, which explains why we find a slightly higher $|\partial P_{\text{CR}}/\partial x|$ value. On the other hand, when integrated over the momentum range of $0.1p_0 < p < 10p_0$, we obtain the value of CR pressure gradient to be 2.48×10^{-7} . We can interpret this find as particles over this momentum range accounts for most of the wave excitation and CR scattering.